Journal of Sea Research 182 (2022) 102188

Contents lists available at ScienceDirect

Journal of Sea Research

journal homepage: www.elsevier.com/locate/seares

Spatiotemporal variations of the thermohaline structure and cyclonic response in the northern Bay of Bengal: The evaluation of a global ocean forecasting system

Shaila Akhter[a,b,c,d], Fangli Qiao[c,e,f,*], Kejian Wu[a,b], Xunqiang Yin[c,e,f], K. M. Azam Chowdhury[g], Md Kawser Ahmed[g], A.S.M. Maksud Kamal[h]

[a] *College of Oceanic and Atmospheric Sciences, Ocean University of China, Qingdao 266100, China*
[b] *Physical Oceanography Laboratory, Ocean University of China, Qingdao 266100, China*
[c] *First Institute of Oceanography, Ministry of Natural Resources, Qingdao 266061, China*
[d] *Bangladesh Betar, Ministry of Information and Broadcasting, Government of the People's Republic of Bangladesh, Dhaka 1207, Bangladesh*
[e] *Laboratory for Regional Oceanography and Numerical Modeling, Qingdao Pilot National Laboratory for Marine Science and Technology, Qingdao 266237, China*
[f] *Key Laboratory of Marine Science and Numerical Modeling, Ministry of Natural Resources, Qingdao 266061, China*
[g] *Department of Oceanography & International Centre for Ocean Governance (ICOG), University of Dhaka, Dhaka 1000, Bangladesh*
[h] *Department of Disaster Science and Management, University of Dhaka, Dhaka 1000, Bangladesh*

A R T I C L E I N F O

Keywords:
Ocean forecasting system
FIO-COM
Model validation
Tropical cyclone
Titli
Upwelling

A B S T R A C T

Although the performance of the high-resolution global ocean forecasting system, which is based on First Institute of Oceanography surface wave-tide-circulation coupled ocean model (FIO-COM) has been demonstrated to have reasonable accuracy in global context, especially in tropical oceans and some special cases, the assessment needs to be extended in different parts of the global oceans. As such, given the significance of a regional Ocean Forecasting System (OFS) in the world's prominent freshwater dominated basin, the northern Bay of Bengal, a groundwork is crucial for the modeling community. Thus, performance of FIO-COM analysis and forecasting results is assessed by utilizing available moored buoy, satellite, and reanalysis datasets. The present study compares the thermohaline structure related variables (e.g., temperature, salinity) from FIO-COM with aforementioned datasets on a seasonal and daily basis. We focused on evaluating the FIO-COM outputs during a very severe cyclonic storm named *Titli* that formed in October, 2018. The root-mean-square errors (RMSEs) for sea surface temperature (SST) ranges from 0.47 to 0.71 °C, and for sea surface salinity from 0.62 to 0.83 psu; while vertical profile RMSE ranges from 0.27 to 1.0 °C for temperature, and 0.22 to 0.56 psu for salinity between FIO-COM products and observations. Daily variations in different thermohaline structure related variables at two RAMA positions are also well captured by the FIO-COM outputs. Both model and satellite data show pronounced SST cooling (approximately 2.0–2.5 °C) and increased sea surface salinity (~ 1 psu) on the right side of the cyclone track. High SST, TCHP and deep isothermal layer depth were the main oceanic triggering forces to intensify the cyclone *Titli*.

1. Introduction

Understanding ocean circulation patterns and major oceanographic variables such as temperature, salinity, ocean currents, surface waves, tides, sea level, etc., are mandated for ocean and climate forecasting and sustainable planning of maritime activities in coastal and offshore areas (Mehra and Rivin, 2010; Francis et al., 2013; Chakraborty and Gangopadhyay, 2016a). Accurate forecasting of these aforementioned oceanographic variables is necessary for various purposes, including but not limited to ensuring safe navigation, identifying the increased maritime activities such as shipping and fishing in high-productive areas suitable harvesting time, early warning for coral bleaching; providing oil spill advisory services, assisting in search and rescue operations, mitigating storm damage and flooding in coastal areas, and improving climate prediction in response to global warming (Francis et al., 2013; Kourafalou et al., 2015; Chakraborty and Gangopadhyay, 2016b;

* Corresponding author at: First Institute of Oceanography, Ministry of Natural Resources, Qingdao 266061, China.
E-mail address: qiaofl@fio.org.cn (F. Qiao).

https://doi.org/10.1016/j.seares.2022.102188
Received 4 December 2021; Received in revised form 22 January 2022; Accepted 1 March 2022
Available online 5 March 2022
1385-1101/

Francis et al., 2020). As a result, the ocean forecasting system (OFS) serves all kinds of end-users, from traditional fishermen to high-tech marine industries.

Recognizing the importance of OFS, many countries around the world, including Australia (Bluelink ocean forecast system) (Brassington et al., 2007), Japan (Multivariate Ocean Variational Estimation system) (Usui et al., 2006), United States (Hybrid Coordinate Ocean circulation Model) (Hurlburt et al., 2008), Italy (Mediterranean ocean Forecast System, MFS), Norway (Forecasting Ocean Assimilation Model, FOAM), France (Mercator Océan), United Kingdom (FOAM), India (High-resolution Operational Ocean Forecast and reanalysis System), and China (First Institute of Oceanography Coupled Ocean Model, FIO-COM) have established operational OFS for providing services to the world. The skill and accuracy of these forecasting systems vary due to different numerical models with varied model configurations, contrasting data assimilation methods, distinct atmospheric forcing and oceans' open boundary conditions, and so on (Wang et al., 2018).

The IOC/WESTPAC OFS is based on surface wave-tide-circulation coupled ocean model developed by the First Institute of Oceanography, Ministry of Natural Resources of China (Qiao et al., 2019). FIO-COM has been providing ocean forecasting services to ocean communities all over the world since December 10, 2018 through the official website of IOC/WESTPAC. The MOM5 (Modular Ocean Model, Version 5) ocean circulation model (Griffies, 2012), the MASNUM (Marine Science and Numerical Modeling) surface wave model (Qiao et al., 2016a), and the sea ice simulator ice model (Winton, 2000) are the foundations of FIO-COM. The FIO-COM is a high resolution global model with a horizontal resolution of $0.1^\circ \times 0.1^\circ$ and 54 vertical layers. The K-profile parameterization (KPP) vertical mixing scheme was adopted in the FIO-COM including the non-breaking surface wave-induced mixing (Bv). The parameterization of Bv is developed by Qiao et al. (2004, 2008, 2010, 2016b), which can considerably improve upper ocean simulation capacity (Shu et al., 2011; Wu et al., 2015). To analyze the mixing impacts of tides, the parameterized tide-induced mixing is also incorporated in the FIO-COM from a global tide model with eight major tidal constituents (Xiao et al., 2016), which turns the FIO-COM a surface wave-tide-circulation fully coupled ocean model.

The FIO-COM analysis data is assessed in the tropical oceans and confirmed to be of high quality (Sun et al., 2020). The performance of FIO-COM forecasting products has also been validated to be excellent, attracting a lot of interests from different countries. For instance, the successful application of the prediction results of the *Sanchi* oil spill happened on January 6, 2018, and search and rescue operations at ship accidents in Phuket, Thailand on July 5, 2018 (Qiao et al., 2019) are examples of the prediction ability of FIO-COM. However, the assessment of FIO-COM outputs needs to be extended in different parts of the global oceans (Sun et al., 2020). The northern Bay of Bengal is a freshwater dominant basin with the world fourth largest river system, Ganges-Brahmaputra-Meghna (GBM) (Akhil et al., 2014). This bay is exposed to sea level rise (Akhter et al., 2021), and severe tropical cyclones are very common during pre- and post-monsoon (Anonymous, 1979; Obasi, 1997) causing large-scale flooding and destruction along the coastal belts. Therefore, as part of the assessment of FIO-COM analysis and forecasting results, the northern Bay of Bengal is the selected domain for this paper.

Bangladesh has 710 km of exposed coastline along the northern Bay of Bengal (Allison, 1998). However, Bangladesh has been lacking of an OFS despite its vital geographic, economic, natural catastrophe, and scientific interests. The recently acquired vast sea space (Ministry of Foreign Affairs, MoFA, 2014) could be effectively utilized and the natural disaster could be well-predicted by establishing an operational OFS. An operational OFS will also accelerate the blue economic growth in Bangladesh by assuring maritime safety and security for people and conserving the marine environment. The current study would serve as a ground work to develop a regional OFS for the northern Bay of Bengal.

The present study compares the temperature, salinity, and some relevant variables in the water column (e.g., mixed layer, barrier layer, and heat content etc.) of FIO-COM with the observational and satellite datasets on a seasonal and daily basis. Finally, *Titli*, a very severe cyclonic storm that hit India on October, 2018, was adopted to verify the forecasting accuracy and the upper ocean response (due to cyclone) of FIO-COM in the northern Bay of Bengal (Fig. 1a).

2. Data and method

2.1. Data sources

Sea surface temperature (SST): We utilized Optimum Interpolation Sea Surface Temperature (OISST; version 5.0) data from remote sensing systems (www.remss.com), which combines microwave (MW) and infrared (IR) datasets known as MW_IR. Microwave sensors include TMI, AMSR-E, AMSR-2, WindSat, and GMI, whereas infrared sensors include MODIS-Terra, MODIS-Aqua, and VIIRS-NPP. The horizontal resolution is 9 km and temporal resolution is daily.

Sea surface salinity: This study used sea surface salinity from Soil Moisture Active Passive (SMAP) (version 4.0, level 3) with 8-Day running mean gridded product. This product is based on the fourth release of the NASA SMAP observatory's validated standard mapped sea surface salinity data, which was created operationally by remote sensing systems. The horizontal resolution of this product is 70 km. The original data has been interpolated to a geographic resolution of 0.25° by 0.25° and can be downloaded from http://www.remss.com/missions/smap.

Temperature and salinity profile data: Temperature and salinity data from Argo profiling floats (Argo, 2000) in the northern Bay of Bengal have been obtained from the Global Ocean Data Assimilation Experiment (GODAE) project (http://www.argo.ucsd.edu). Argo floats data was utilized in the period of 6th and 12th October, 2018. The position of the seven Argo floats available in the study domain during this period are placed in Fig. 1b with their IDs.

Observational temperature and salinity profiles from RAMA buoy (McPhaden et al., 2009b) are utilized in this study. Daily data from the two RAMA buoys (marked as yellow circle in Fig. 1b) located in the northern Bay of Bengal at position (15°N, 90°E) and (12°N, 90°E) are downloaded for the year 2018. At position (12°N, 90°E), RAMA buoy data were available from January to June (181 days).

Temperature and salinity gridded data: This study uses a new version of the EN4 series ocean objective analysis product (EN4) from the UK Met Office Hadley Centre for the year 2018, with temperature data from the Expendable Bathythermograph (XBT) corrected using the Gouretski and Reseghetti scheme (2010). The EN4 monthly potential temperature and salinity fields are utilized, which have a horizontal resolution of 1° by 1° and a vertical resolution of 42 levels from sea surface (5 m) to 5500 m. To make comparable with EN4 data, the starting depth of FIO-COM output is also considered from 5 m. In-situ observations in the EN4 series came from the World Ocean Database (WOD13) (Boyer et al., 2013), the Global Temperature-Salinity Profile Program (GTSPP), the Array for Real-time Geostrophic Oceanography (Argo), and the Arctic Synoptic Basin-wide Observations (ASBO) (Levitus et al., 2009; Good et al., 2013).

Wind speed: The National centers for environmental prediction of USA (NCEP) operates a weather forecast model Global Forecast System (GFS, analysis and forecasting datasets), which provides 3-hourly air temperature, atmospheric pressure on the sea surface, ocean surface wind at 10 m height, the precipitation, specific humidity and heat flux. The atmospheric forcing for the FIO-COM model comes from the GFS datasets. The data are available at http://ncss.hycom.org/thredds/ncss/grid/GLBu0.08/expt_91.2/dataset.html, with horizontal resolution of $0.25^\circ \times 0.25^\circ$. In this study surface wind at 10 m height product of GFS are considered for October, 2018 to observe the intensity of wind and to estimate the Ekman pumping velocity.

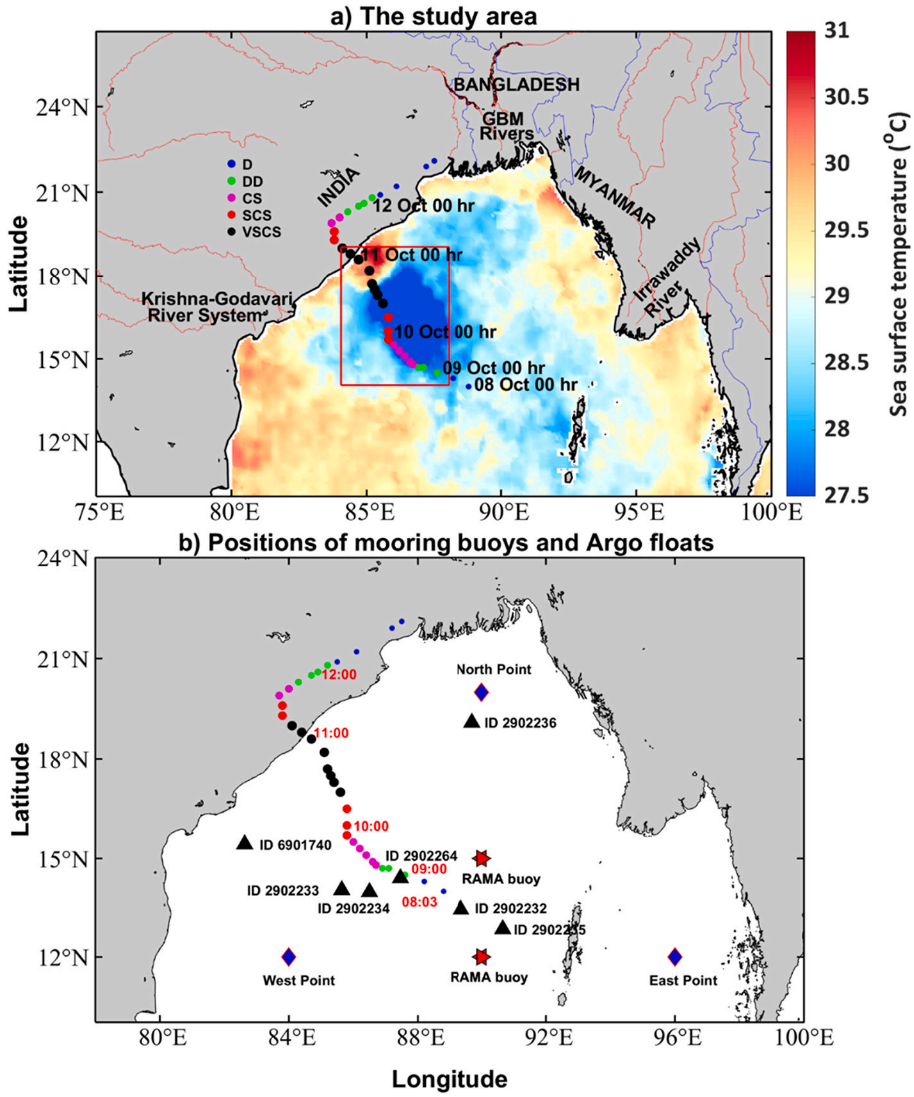

Fig. 1. (a) Distribution of SST (°C) (shading) of Optimum Interpolation Sea Surface Temperature from microwave and infrared data sources in the study domain (78° - 100°E, 10° - 24°N) on 10th October (with very severe cyclone). The red lines represent major rivers, the black lines represent coasts. The three-hourly positions of cyclone '*Titli*' (IMD, 2018) are indicated by filled circles of different colors, depending on the category (using Saffir-Simpson hurricane wind scale). Here, D, DD, CS, SCS, VSCS stands for depression, deep depression, cyclonic storm, severe cyclonic storm and very severe cyclonic storm, respectively. The area within the red rectangular box is considered to check the sensitivity of model forecasting to cyclone '*Titli*'. **(b)** Locations of seven Argo floats are marked with black filled upper triangles. The Research Moored Array for African-Asian-Australian Monsoon Analysis and Prediction (RAMA) buoys are located in the filled red asterisk. The locations where the temperature and salinity profiles from FIO-COM output are compared with EN4 data of Met Office Hadley Centre are shown by three diamonds filled with blue color. (For interpretation of the references to color in this figure legend, the reader is referred to the web version of this article.)

2.2. Methods

Based on annual cycles of heat and freshwater fluxes, four seasons are considered in this analysis following Thadathil et al. (2007) and Narvekar and Prasanna Kumar (2014): winter (November–February), spring (March–May), summer (June–August), and autumn (September–October). The daily mixed layer depth (MLD) (bottom depth of the mixed layer), isothermal layer depth (ILD) (a uniform temperature layer), tropical cyclone heat potential (TCHP), and ocean heat content are calculated using temperature and salinity data from the RAMA buoy, and then compared with the analysis and forecasting datasets of FIO-COM. These parameters are also calculated from the analysis datasets of FIO-COM outputs and Argo floats before and after cyclone period.

Calculation of ILD and MLD: The criterion adopted for determining the ILD is a 0.8 °C drop in temperature from the surface to the subsurface (Wyrtki et al., 1971; Sprintall and Tomczak, 1992; Masson et al., 2002; Rao and Sivakumar, 2003; Thadathil et al., 2007, 2016; Shee et al., 2019). MLD is determined using the density in water column calculated from model and Argo temperature and salinity data. MLD is computed in terms of depth, with a density equal to that at the surface plus a density increment equal to a 0.8 °C reduction in temperature (see Eq. 1) (Kara et al., 2000; Rao and Sivakumar, 2003; de Boyer Montégut et al., 2004; Thadathil et al., 2007; Kumari et al., 2018; He et al., 2020; Chowdhury et al., 2021b). Hence, the increment of the density is as follows:

$$\Delta\sigma = \sigma_t(\mathrm{SST} + \mathrm{dT}, \mathrm{SSS}, \mathrm{P}_0) - \sigma_t\,(\mathrm{SST}, \mathrm{SSS}, \mathrm{P}_0) \quad (1)$$

Where, $\Delta\sigma$ is the density difference between the surface and the MLD; σ_t is the potential density (kg m^{-3}) calculated from the temperature, salinity and reference pressure; and dT is 0.8 °C.

A barrier layer is an isothermal salinity-stratified layer positioned just below the MLD and above the bottom of ILD (Girishkumar et al., 2013; Pant et al., 2015; Kumari et al., 2018), and the thickness of the barrier layer is the barrier layer thickness (BLT). Thus, the difference between ILD and MLD is used to calculate BLT in this study.

Calculation of the TCHP and ocean heat content: TCHP and ocean heat content are usually used to quantify the frequency and intensification of tropical cyclones (Sadhuram et al., 2004). As tropical cyclones initiate in oceanic regions with SST above 26 °C, following Goni et al. (2009), the integrated vertical temperature change from the sea surface to the depth of the 26 °C isotherm (D26) is considered to be the TCHP and is determined as follows:

$$\mathrm{TCHP} = \rho\,\mathrm{Cp}\int_0^{\mathrm{D26}}[\mathrm{T(Z)} - 26]\,\mathrm{Dz} \quad (2)$$

To calculate the ocean heat content in the upper layer of this bay, the depth from the surface to the 23 °C isotherm (D23) is considered here, as we assume that the seasonal influence is mostly prolonged up to this depth. The 23 °C isotherm extends to approximately 100 m to 120 m depth, and the thermocline below this depth can be regarded as a quasi-permanent thermocline. Ocean heat content is defined as follows:

$$\text{Ocean heat content} = \rho\, \mathrm{Cp} \int_0^{D23} [\mathrm{T}(\mathrm{Z})]\, \mathrm{dz} \tag{3}$$

In the above equations, T(z) is the temperature (°C) of each layer of thickness "dz", ρ is the density of seawater as a function of depth, C_p (3989.2 J kg^{-1} °C) is the specific heat capacity of seawater.

Ekman pumping velocity: Wind fields above 10 m height from ocean surface derived from GFS data is utilized to analyze spatial wind fields around the cyclone track. The Ekman pumping velocity is calculated using the following formula

$$\text{Ekman pumping velocity} = \frac{1}{\rho \mathrm{f}} (\nabla \times \tau) \tag{4}$$

Where, ρ is density of sea water, τ is wind stress, and f is Coriolis parameter.

Root Mean Square Error (RMSE): RMSE compares a predicted value and an observed or known value. The smaller an RMSE value, the better prediction or forecasting ability. RMSE is defined as follows:

$$\mathrm{RMSE} = \sqrt{\frac{\sum_{I=1}^{N} (X_I - \dot{X}_I)^2}{N}} \tag{5}$$

In these equations, I is individual non-missing data points, N is number of non-missing data points, X_I is time series of actual observations, and $\dot{X}_I$ is estimated time series.

3. Inter-comparison of the FIO-COM result with observations

3.1. Verification of the seasonality of temperature and salinity

The SST is a crucial parameter for understanding the upper-ocean thermodynamics, circulation, and air-sea interactions (Schott et al., 2009; Zhu et al., 2018). SST is also a good predictor in a hydrostatic ocean general circulation model, hence SST bias is one of the main elements for evaluation of numerical modeling skills. Many factors contribute in the SST simulation error, including the constraint of the physical model, the quality of the surface atmosphere, the uncertainty of the initial field, the open boundary, and subsurface mixing (Qiao et al., 2004; Ji et al., 2015; Sun et al., 2020).

SST in the Bay of Bengal exhibits considerable seasonal changes, with two peaks in May and October, due to its subtropical location and accompanying air-sea interactions, as well as its role in feeding massive river discharge and rainfall during the summer (Pant et al., 2015; Akhter et al., 2021). The spatial distributions of seasonal SST in the northern Bay of Bengal of EN4 data and FIO-COM model output are displayed in Fig. 2. EN4 SST has strong seasonal variation with two peaks. It remains low in winter and reaches the highest value in spring (Figs. 2 a1-b1). During summer, it remains high and again reaches a peak in autumn (Figs. 2 c1-d1). The model accurately reproduces the seasonal pattern of SST across the basin and is reasonably comparable to that of EN4 data, with basin averaged RMSE ranging from 0.47 to 0.71 °C (Figs. 2 a2-d2). However, the model SST is a bit lower during the winter and marginally higher during the other seasons when compared to EN4 data near the northern coast of the bay, which is the freshwater much influenced zone (Figs. 2 a3-d3). Freshwater driven stratification could explain the variation in SST along the bay's estuaries and coastal areas, and RMSE of less than 1.0 °C is plausible in this bay (Behara and Vinayachandran, 2016; Jana et al., 2018).

The spatial distribution of sea surface salinity from EN4 data shows a contrasting pattern with comparatively fresher water in the northern tip than other part of the northern Bay of Bengal (Figs. 3 a1-d1). Although the negative gradient of sea surface salinity exists from north to south all the year round, a strong seasonal variation is discernible in the observed sea surface salinity. During spring (pre-monsoon period), the low sea surface salinity (less than 32) confined to the northeastern part of the bay, which is discernible from EN4 data (Fig. 3 b1). However, during summer (monsoon) the northern part of the bay overwhelms with the freshwater, which gradually spreads towards the south (Fig. 3 c1). Some of this monsoonal freshwater is retained throughout the winter, but it retreats in the spring and is confined to the northernmost tip (Figs. 3 a1-b1), as reported by Akhil et al. (2014).

The model accurately reproduces the spatial distribution of seasonal

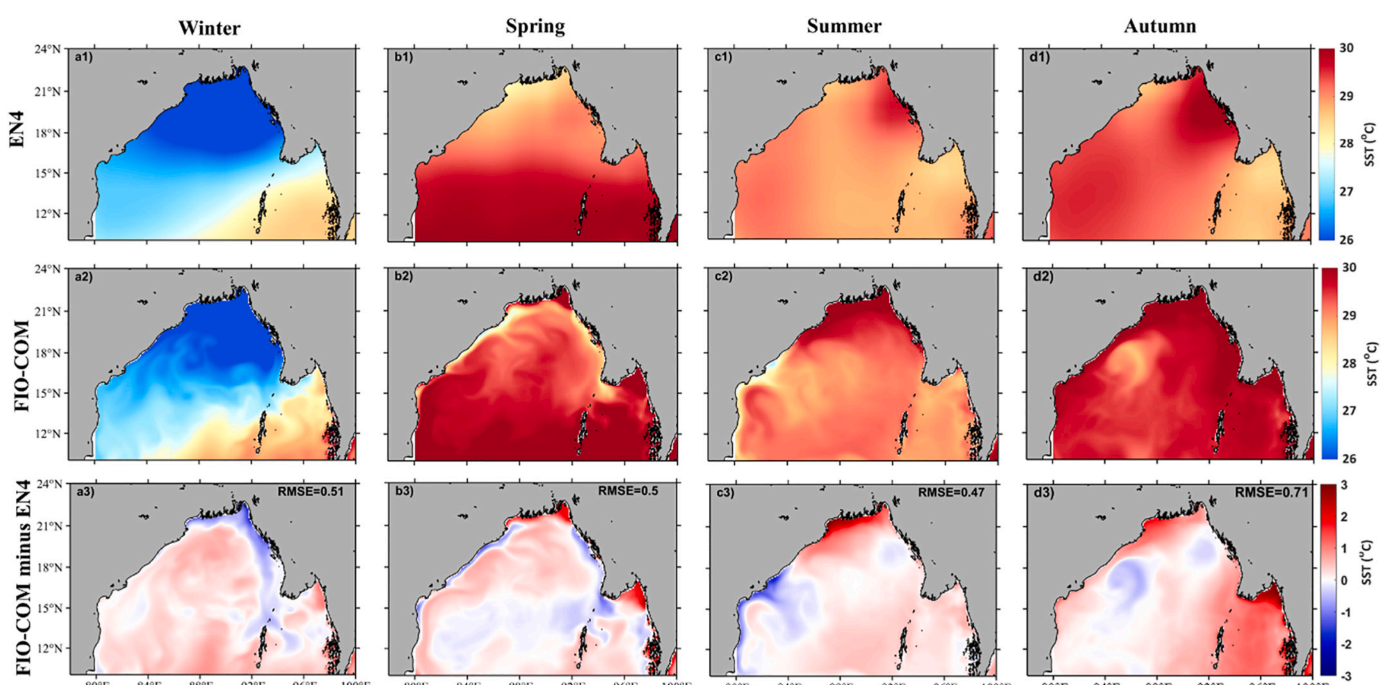

Fig. 2. Variation of SST (°C) during winter (a1, a2), spring (b1, b2), summer (c1, c2), and autumn (d1, d2) from EN4 and FIO-COM, respectively. The biases of FIO-COM SST (°C) against EN4 during winter (a3), spring (b3), summer (c3), and autumn (d3).

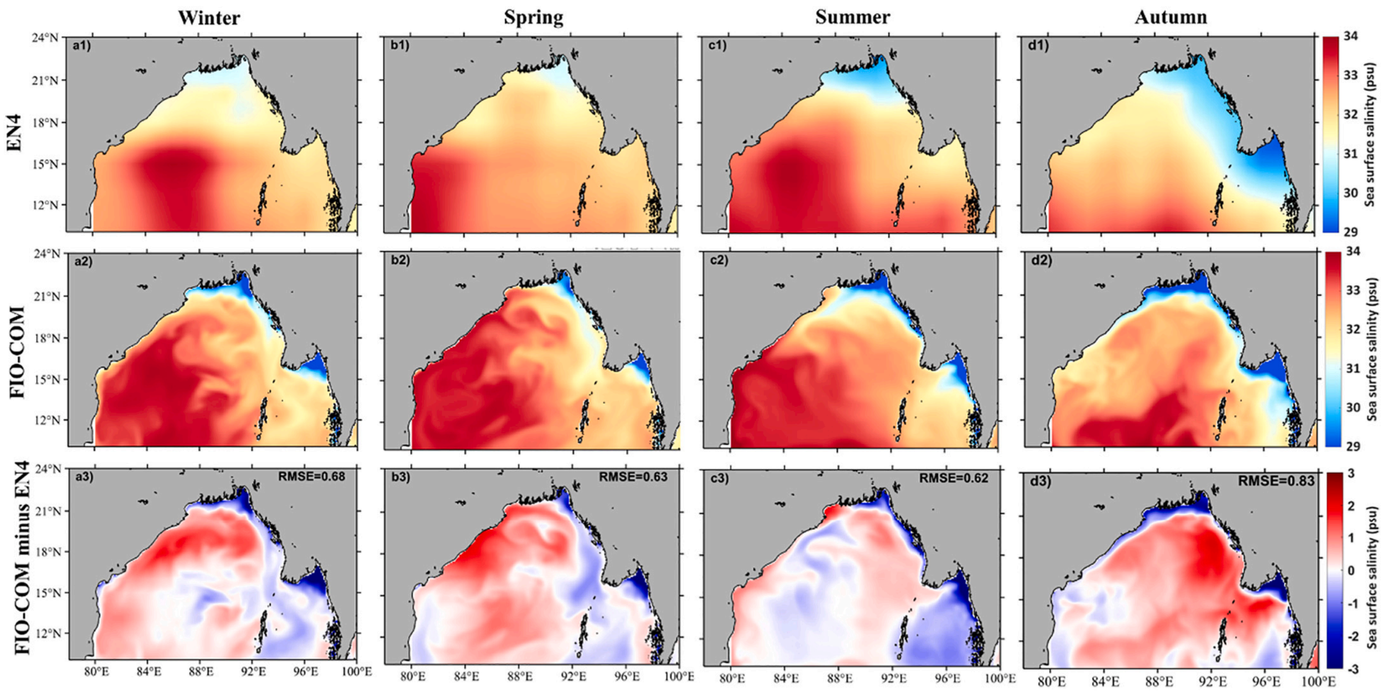

Fig. 3. Variation of sea surface salinity (psu) during winter (a1, a2), spring (b1, b2), summer (c1, c2), and autumn (d1, d2) from EN4 and FIO-COM, respectively. The biases of FIO-COM sea surface salinity (psu) against EN4 during winter (a3), spring (b3), summer (c3), and autumn (d3).

sea surface salinity exhibited by EN4 data (Figs. 3 a2-d2). The model, like EN4 data, can accurately reflect the commencement and dispersion of freshwater pathways, particularly the spread of monsoonal freshwater along the eastern and western coasts (Figs. 3 c2-d2). During the summer and autumn, the extreme freshness along the major freshwater contributor, the GBM River system, is well depicted by the model simulation. The freshwater input from the mighty Irrawaddy River along the tip of Andaman Sea is also well captured by the model results. However, the simulated sea surface salinity is slightly higher to some extent offshore of the bay, with RMSE varying from 0.62 to 0.83 psu throughout the year and larger RMSE in the autumn (RMSE 0.8 psu) (Figs. 3 a3-d3). Estimation of more realistic salinity is still challenging in this area, which is renowned for having large freshwater (Howden and Murtugudde, 2001; Vinayachandran et al., 2002; Sengupta et al., 2006; Akhil et al., 2014). For example, coupled models exhibit high salinity biases (~1.5 psu) over the Bay of Bengal (Vinayachandran and Nanjundiah, 2009; Fathrio et al., 2017).

Vertical profiles of seasonal temperature and salinity in the northern, western, and eastern parts of the Bay of Bengal (see Fig. 1b for locations) are analyzed. Existence of temperature inversion (increase of subsurface temperature compared to surface by certain degrees) in the northern Bay of Bengal during winter is reported earlier (Thadathil et al., 2016; Li et al., 2016; Chowdhury et al., 2021a). Temperature inversion appeared in both the FIO-COM model and the observations during the winter at the northernmost location (Fig. 4 a1). Vertical profiles of temperature from FIO-COM show the similar seasonal pattern of EN4 in the year-round in all three locations with RMSE from 0.27 to 0.77 °C (Fig. 4, Table 1). However, a bit more RMSE of ~1.0 °C appears during summer at the northern point and autumn at the eastern point (Figs. 4 c1, d3). In the Bay of Bengal, Chakraborty and Gangopadhyay (2016a) used a high resolution ROMS model simulation and reported RMSE of 1.0 to 2.3 °C, particularly in the thermocline depths. The model bias of approximately 1 °C in the subsurface temperature is also reported in the study of Jana et al. (2015). Capturing the thermocline precisely compared to observation/reanalysis data is still a great challenge in modeling community. However, FIO-COM as a global ocean model can capture the subsurface temperature very well even better than the result of existing regional models. Inadequate mixing in ocean models is a common problem for nearly all ocean circulation models (Ezer, 2000; Huang et al., 2011; Huang and Qiao, 2010; Mellor, 2003), while FIO-COM has taken advantage of the non-breaking surface wave-induced mixing, which has led in more realistic thermocline results (Qiao et al., 2004, 2010; Wu et al., 2015).

The vertical profiles of the salinity at three regions of the bay show seasonal trend similar to EN4 (Fig. 4) with a RMSE varying from 0.11 to 0.56 psu (Table 1). In all salinity profiles, bias is found predominantly from the surface to a depth of 100 m. The bias in salinity profiles is the highest at the northern point (RMSE from 0.22 to 0.56 psu), and the intermediate at the eastern point (RMSE from 0.20 to 0.38 psu), and the lowest at the western point (RMSE from 0.11 to 0.15 psu).

3.2. Verification of the different parameters at RAMA buoy's position on daily basis

Daily vertical temperature and salinity profiles from RAMA moored buoy's data are used to get SST, sea surface salinity, ILD, MLD, BLT, D26, TCHP and ocean heat content at positions (15°N, 90°E) and (12°N, 90°E). The aforementioned characteristics are also computed from FIO-COM outputs for analysis day as well as for day-1 and day-3 lead time forecasting, and then displayed against RAMA buoy data for comparison (Figs. 5 and 6).

If other ambient conditions are favorable, the gradient in the SST field is crucial for detecting the high biological production zone (e.g., likelihood of increased fish catches, region of upwelling) (Rajeevan et al., 2012; Yang et al., 2007). As a result, accurate SST prediction becomes critically important in operational OFS (Schott and McCreary Jr, 2001; Schott et al., 2009). Daily variation in SST pattern from FIO-COM model are in good agreement with the RAMA buoy observation at (15°N, 90°E) with low root mean square error (RMSE ~0.41 °C) (Fig. 5a). In the northern Bay of Bengal, FIO-COM SST forecasting with 1-day and 3-day leads is also very compatible with RAMA buoy's data. The RMSE for 1-day and 3-day lead-time at (15°N, 90°E) are 0.42 °C and 0.42 °C, respectively, at (12°N, 90°E) are 0.30 °C and 0.31 °C, respectively (Figs. 5a-6a). Therefore, the precision of the forecasted SST varies

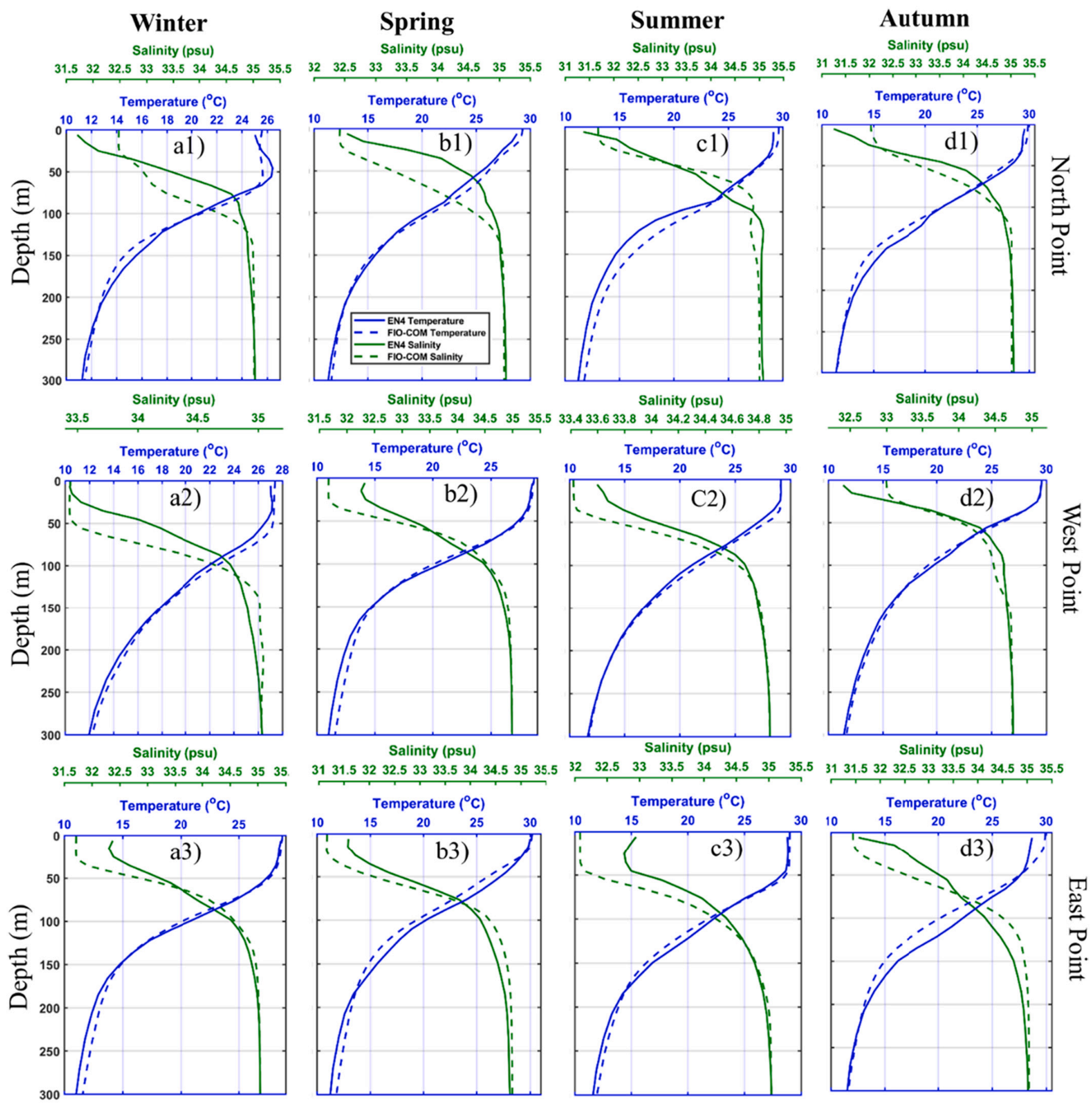

Fig. 4. Variation of sea temperature (°C) and sea salinity (psu) during winter (a1, a2, a3), spring (b1, b2, b3), summer (c1, c2, c3), and autumn (d1, d2, d3) from EN4 and FIO-COM along the north, west and east points, respectively. Observational data is marked with solid line and FIO-COM output is marked with dash lines.

Table 1
RMSE between FIO-COM and EN4 datasets for temperature (°C) and salinity (psu) profiles at three different points of study area.

Area	Winter		Spring		Summer		Autumn	
	Temperature (°C)	Salinity (psu)	Temperature (°C)	Salinity (psu)	Temperature (°C)	Salinity (psu)	Temperature (°C)	Salinity (psu)
North	0.48	0.41	0.43	0.56	1.02	0.22	0.61	0.25
West	0.62	0.15	0.66	0.13	0.34	0.11	0.27	0.13
East	0.44	0.26	0.77	0.2	0.44	0.36	1.1	0.37

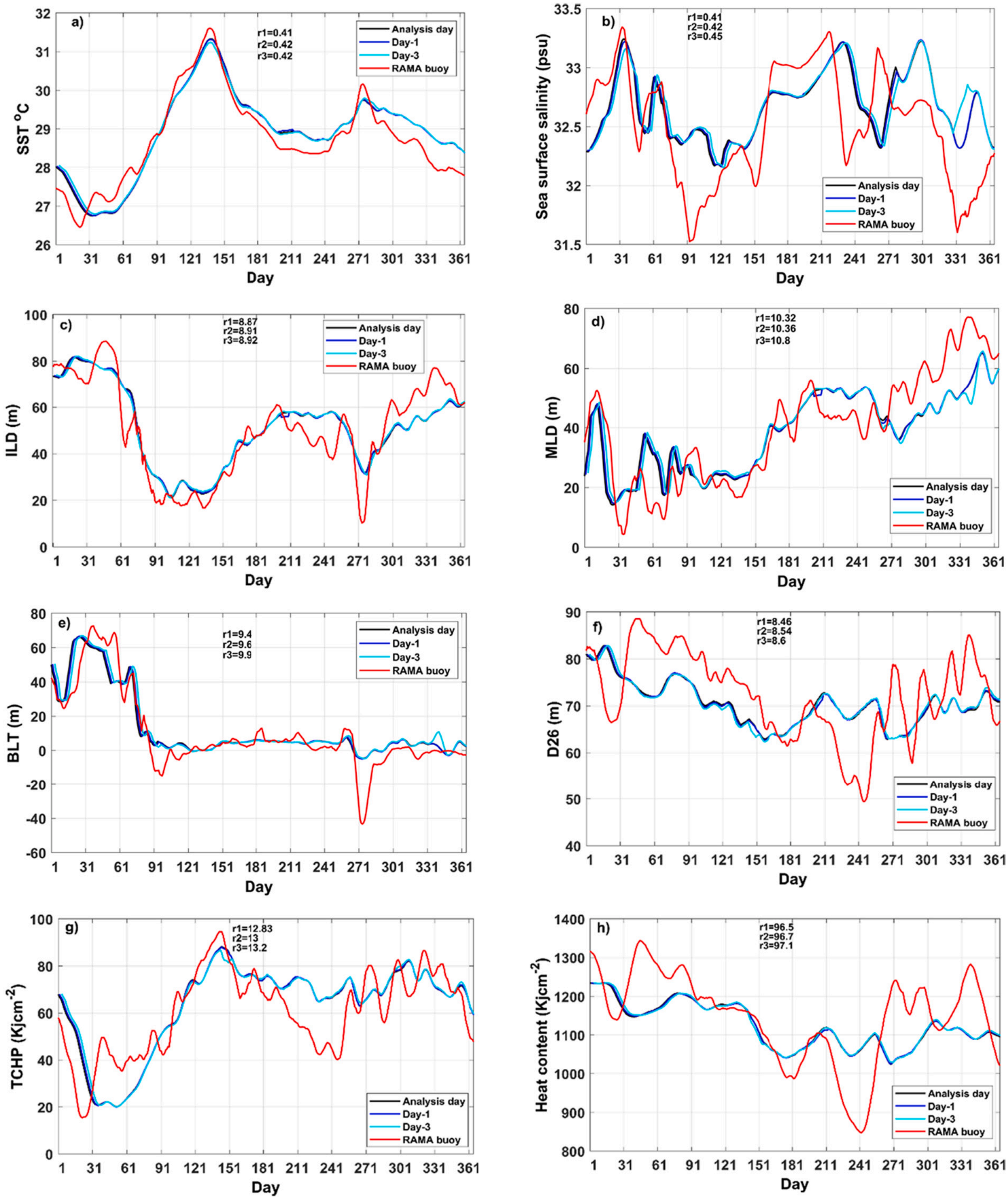

Fig. 5. The 7-days running mean time series of SST (°C) (a), Sea surface salinity (psu) (b), ILD (m) (c), MLD (m) (d), BLT (m) (e), D26 (m) (f), TCHP (Kjcm^{-2}) (g), and heat content (Kjcm^{-2}) (h) forecasted from FIO-COM for various lead time compared with the RAMA observation at (15°N, 90°E). r1, r2 and r3 are the RMSEs' for analysis day, 1-day lead time and 3-day lead time, respectively.

by location, with the southern part of the northern Bay of Bengal at (12°N, 90°E) having comparatively better accuracy than the northern part of the bay at (15°N, 90°E).

As a freshwater dominant basin, daily sea surface salinity variation becomes a crucial variable in the northern Bay of Bengal. Although the daily sea surface salinity variations from the model in the southern part of the northern Bay of Bengal at (12°N, 90°E) agree well with observation (RMSE ranges from 0.20 to 0.22 psu) (Fig. 6b), the northernmost RAMA buoy position at (15°N, 90°E) has a comparatively higher RMSE of 0.41, 0.42, and 0.45 psu for analysis day, 1-day to 3-day lead, respectively (Fig. 5b). There are many small rivers that falls in the northern Bay of Bengal (Jana et al., 2018, Chowdhury et al., 2021a). Inclusion of these small rivers in the model input besides the GBM and other major river systems might improve the accuracy of salinity simulation. Consequently, the ocean modeling community is still struggling to figure out the appropriate inclusion of river inputs into models (Jensen et al., 2016; Jana et al., 2018; Masud-Ul-Alam et al., 2022).

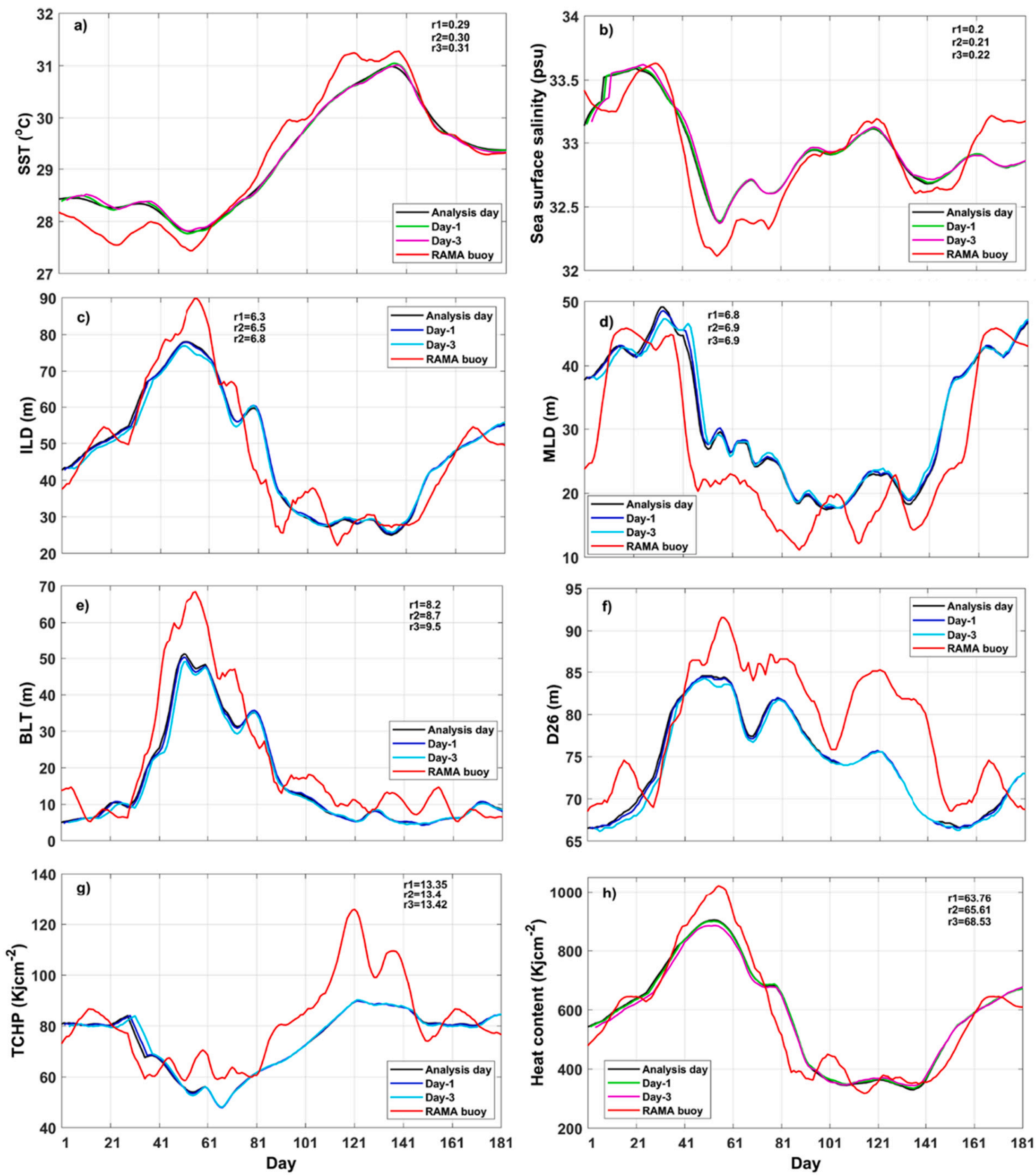

Fig. 6. Same as Fig. 5 but at (12°N, 90°E).

The mixed layer, as the interface between the atmosphere above and the water below, is important to air-sea interaction processes (Foltz et al., 2003; Lee et al., 2015). The MLD is mostly determined by salinity and wind mixing throughout the year (Felton et al., 2014; Akhter et al., 2021). Freshwater induces substantial density stratification in the upper ocean of the Bay of Bengal, shoaling the MLD, while Ekman pumping deepens the ILD (Thadathil et al., 2007; Shetye et al., 1996; McCreary et al., 1996). The BLT becomes deep in the Bay of Bengal during the winter, when low saline waters from precipitation and river runoff are redistributed across the Bay, causing high upper ocean stratification (de Boyer Montégut et al., 2007; Thadathil et al., 2007; Pant et al., 2015). For good numerical ocean model simulations, an accurate depiction of upper ocean thermohaline structure (i.e., MLD, ILD, and BLT) is required.

The daily variability of the ILD is well captured on analysis day, and predicted days by the model with RMSE approximately 9 m at (15°N, 90°E) and RMSE approximately 6 m at (12°N, 90°E) (Figs. 5c, 6c). Whereas, previously ILD was predicted with comparatively higher error (RMSE ~14 m) in this region (Francis et al., 2013). Model simulated and predicted MLD magnificently follows the daily variation pattern like observation at (12°N, 90°E) with RMSE ~6.8 m (Fig. 6d). However, at (15°N, 90°E) the model simulated MLD is slightly shallower than observations during autumn and winter (Fig. 5d). Model simulated and predicted BLT follow the daily variation pattern like observation at (12°N, 90°E) with RMSE varying from 8.2 to 9.5 m but the trend is followed with low accuracy at (15°N, 90°E) (Figs. 5e, 6e). However, the model accurately captures the thicker BLT of winter (Thadathil et al., 2007) from observation in both RAMA buoy stations (Figs. 5e, 6e). Thus, daily fluctuations in ILD, MLD, and BLT, in particular, accurately capture the seasonal cycle similar to RAMA buoy data in FIO-COM model results.

In the tropics, the depth of the 26 °C isotherm (D26) might be used to identify the top of the thermocline (Sarma et al., 1990; Girishkumar et al., 2013). Although the fluctuations in the depth of thermocline might be of the order of few meters per day, a larger variability in the tropics is generally associated with seasonal or annual cycles driven by large-scale ocean dynamics (Chen and Wang, 2016). The thermocline is an essential indicator of internal ocean thermodynamics because the majority of heat is stored in the water column above the thermocline (Sadhuram et al., 2006). As a result, the quality of simulations using ocean general circulation models is reflected in the accurate modeling of this change in thermocline depth. The daily variation of predicted (1-day and 3-day lead) D26 in two positions of the northern Bay of Bengal are compared with RAMA buoy's observations (Figs. 5f and 6f). The predicted and observed D26 are in good agreement with RMSE of 8.5 m (1-day lead) and 8.6 m (3-day lead) at position (15°N, 90°E). It is comparable with the RMSE of 11 m for 3-day lead prediction of thermocline at position (15°N, 90°E) shown in Francis et al. (2013). The RMSE in 1-day and 3-day leads are 6.4 m and 6.5 m, respectively at position (12°N, 90°E), and this error is substantially smaller than prediction in earlier study (Francis et al., 2013).

SST of more than 28 °C is a potential source of deep atmospheric convection (Shenoi et al., 2002; Thangaprakash et al., 2016) and consequently, tropical cyclone formation in the Bay of Bengal except during the winter (Sadhuram et al., 2006; Thadathil et al., 2016; Kashem et al., 2019). The development of meteorological disturbances such as tropical cyclones and monsoon depressions in this bay is further aided by upper ocean salinity stratification from April to November (Murty et al., 2000). As a result, changes in ocean heat content and TCHP are critical for understanding tropical cyclone genesis. In this study, both the TCHP and ocean heat content from FIO-COM reflect the daily variability quite well compared to RAMA buoy data (Figs. 5g-h, 6g-h).

3.3. Evolution and validation of cyclone '*Titli*'

3.3.1. Synoptic feature of cyclone Titli

Cyclone '*Titli*' passed through the Bay of Bengal (see Fig. 1a for track of cyclone) during October 7 to 13, 2018. *Titli* forms as a low-pressure system over the southeastern Bay of Bengal and neighboring northern Andaman Sea at 0830 IST (Indian Standard Time, IST = Coordinated Universal Time (UTC) + 5:30) on October 7th. This low-pressure system formed a depression over the east-central Bay of Bengal approximately at 0830 IST and strengthened into a deep depression over the east-central Bay of Bengal by 2330 IST on 8 October, with a cyclone-friendly conditions such as high SST, low to moderate vertical wind shear, and upper-level divergence. It became a cyclonic storm named "*Titli*" at 1130 IST on 9 October. At 1130 IST on 10 October, the cyclonic system moved north-northwestwards and continued to intensify into a very severe cyclonic storm. This cyclonic storm maintained its intensity even after landfall near the area (18.80°N, 84.50°E). After landfall, it recurved northeastwards and became weaker around 2330 IST on 11 October. In terms of features such as recurvature after landfall, preserving its destructive power after landfall, and recurvature away from coastal areas for more than two days, the India Meteorological Department described the formation of *Titli* as the "rarest of rare" event. Despite the fact that the wind speed at the time of landfall was substantially higher than in previous storms, human lives were lost significantly fewer due to cyclone *Titli*.

3.3.2. Verification of SST and sea surface salinity during cyclone

The SST was identified to be a key factor in the formation and evolution of tropical cyclones (Bender et al., 1993; Mahapatra et al., 2007). Palmen (1948) was the first to show that practically all hurricanes form over oceans with minimum SST of 26 °C or higher. While higher ambient SST can lead to stronger tropical cyclones, cyclone intensity is much affected by SST cooling near the storm's center (Schade, 2000). Due to this cooling, the overall enthalpy flux delivered to the atmosphere get reduced, which eventually hampers cyclone intensification (Cione and Uhlhorn, 2003). Under the track of the powerful tropical cyclones, the SST decreases by several degrees Celsius as the ocean mixed layer deepens during cyclone. The maximum cooling was observed in the wake to the rear of the tropical cyclones and adjacent to its track. Depending on the strength and route of the cyclones, a 0.3 °C to 3.0 °C reduction in SST is expected across the Bay of Bengal (Rao, 1987; Gopalakrishna et al., 1993; Chinthalu et al., 2001; Subrahmanyam et al., 2005; Sengupta et al., 2007; Kashem et al., 2019).

Fig. 7 shows the evolution of SST during cyclone '*Titli*'. The SST from FIO-COM model (Figs. 7 c1-c5 and 7 d1-d4) is compared with the SST from MW_IR (Figs. 7 a1-a5 and 7 b1-b4) for corresponding 00 UTC of each day during 9 to13 October of 2018. Fig. 7 (b1-b4 and d1-d4) shows the SST difference for FIO-COM and MW_IR for each day of cyclone compared to 00:00 UTC on 8 October. At the beginning of cyclone '*Titli*', the Bay of Bengal was covered by comparatively warmer water in the upper ocean with SST approximately 30 °C (Figs. 7 a1, c1). McPhaden et al. (2009a) reported that higher SST within a range of 28 to 30 °C is one of the favorable conditions for tropical cyclone formation during the pre- and post-monsoon in the Bay of Bengal. Footprint of '*Titli*' has revealed the SST cooling along the track of cyclone. At 12:00 UTC, on 9 October, the first cooling patch appeared (Figs. 7 b1, d1), which might be associated with weak cold-core eddies. With the increase of the intensity of cyclone on 10 October, the decrease of SST was more than 2 °C, while cooling patch continued to enlarge (Figs. 7 b2, d2). MW_IR also shows the existence of colder surface waters over the same region. Later, on the 11 October, the SST drops by more than 2 °C along the storm track over approximately 4° × 3° (zonal × meridional direction) region (Figs. 7 b3, d3). Meanwhile, the SST cooling reaches on an average approximately 2.5 °C. According to both model and satellite data, the cooling pattern persisted for several days after *Titli* landed. The pattern of SST cooling is fully evident to the right of the cyclone track, following the reports that the largest dips in SST are seen to the right of the tropical cyclone's track in the Northern Hemisphere (Black and Dickey, 2008) and to the left of the track in the Southern Hemisphere (Berg, 2002). The change in the SST pattern derived from the FIO-COM output during cyclone *Titli* is highly comparable to satellite data and has captured the cooling nicely.

Observations in the Bay of Bengal have shown an increase in sea surface salinity during tropical cyclones, in addition to the lowering of the SST (McPhaden et al., 2009a; Maneesha et al., 2012; Vinayachandran et al., 2013). However, rainfall and river discharge from the GBM river system also have a considerable impact on sea surface salinity in this bay during the summer monsoon and thereafter (Sengupta et al., 2006; Papa et al., 2012; Chaitanya et al., 2014). Due to cyclonic strong mixing and interaction between the saltier underlying water and the low salinity surface water, the sea surface salinity is estimated to be saltified (Sengupta et al., 2008).

Fig. 8 shows the sea surface salinity simulated by the FIO-COM model and SMAP satellite data at 00 GMT of each day during 9 to 12 October of 2018. As shown from FIO-COM outputs, the net changes in sea surface salinity generated by cyclone '*Titli*' is consistent with SMAP dataset. Before the storm, FIO-COM outputs show sea surface salinity about 32.09 psu to the north of 14°N latitude (Fig. 8 c1). Sea surface salinity is found to increase throughout the cyclonic storm's path both in model and satellite observation (Figs. 8 b1-b4 and 8d1-d4), presumably as a result of turbulent mixing in the upper mixed layer and entrainment of underlying high saline waters into the mixed layer (McPhaden et al., 2009a). The sea surface salinity increase is the largest in the northwest Bay of Bengal where the maximum net sea surface salinity increase exceeds 1.0 psu (Figs. 8 b3-b4 and 8d3-d4). Increase in sea surface

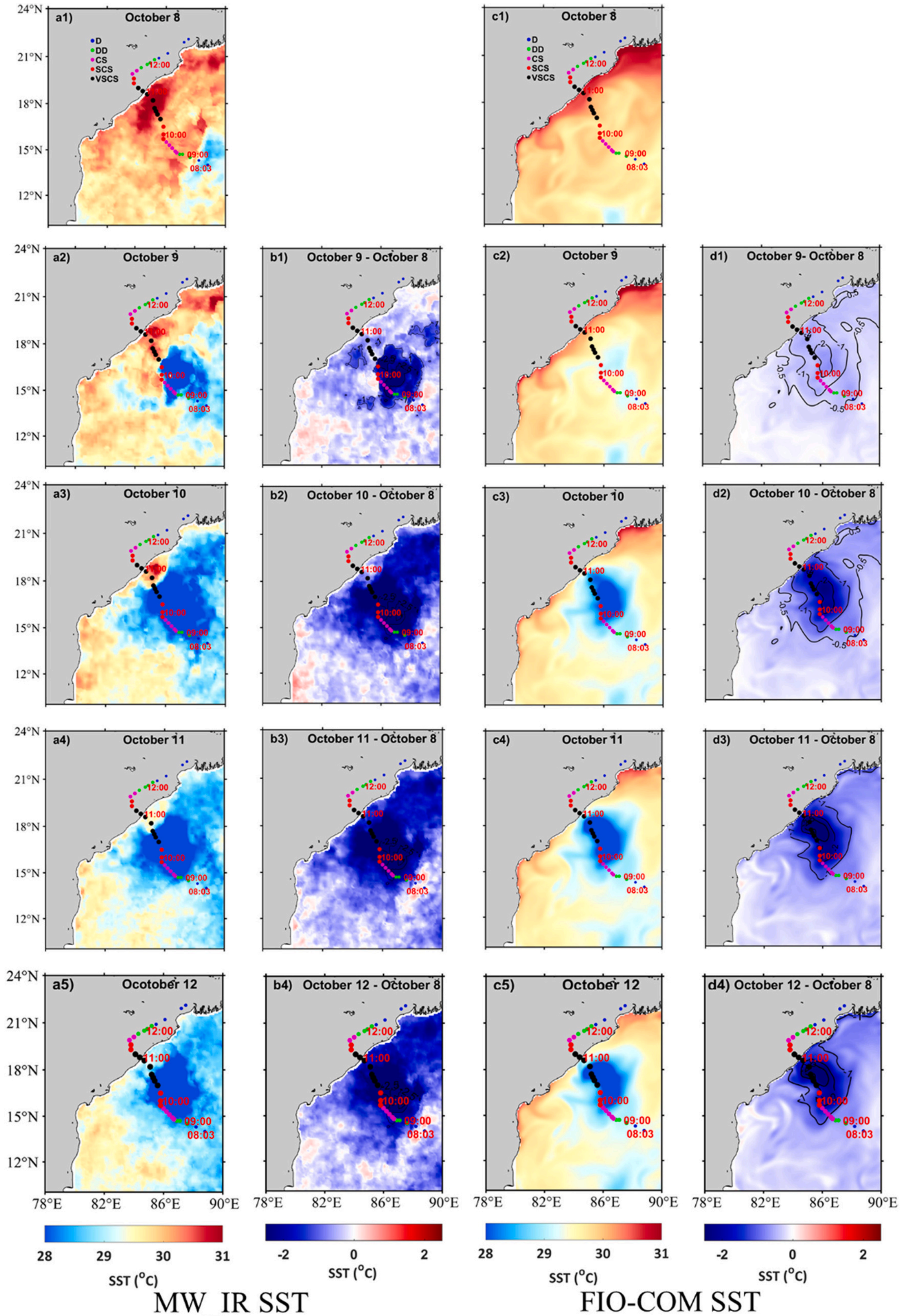

Fig. 7. SST distribution from MW_IR (1st column) and FIO-COM (3rd column) over the cyclone days (8 to 12 October of 2018). SST anomaly computed from MW_IR (2nd column) and FIO-COM (4th column) with contours of anomaly (cyclone days, 9 to 12th October minus initial day of cyclone, 8 October). The numbers in red color indicate the date of cyclone at 00 ISC hour along the track of cyclone. Here, D, DD, CS, SCS and VSCS have the same meaning with those in Fig. 1a. (For interpretation of the references to color in this figure legend, the reader is referred to the web version of this article.)

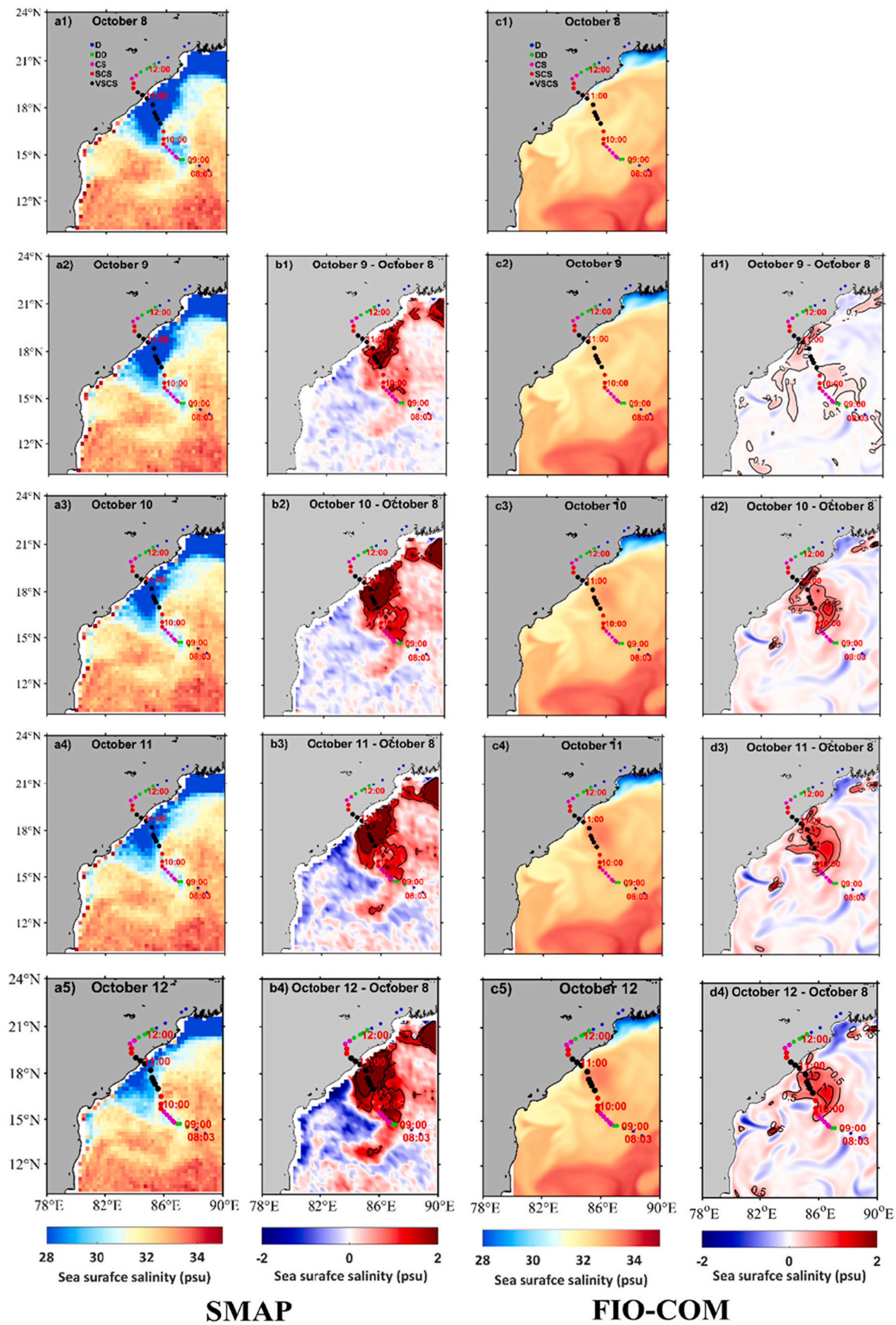

Fig. 8. Sea surface salinity (psu) distribution from SMAP satellite data (1st column) and FIO-COM model (3rd column) over the cyclone days (8 to 12 October of 2018). Sea surface salinity anomaly computed from SMAP (2nd column) and FIO-COM (4th column) with contours of anomaly (cyclone days, 9 to 12 October minus initial day of cyclone, 8 October). The numbers in red color indicate the date of cyclone at 00 h along the track of cyclone. Here, D, DD, CS, SCS and VSCS have the same meaning with those in Fig. 1a. (For interpretation of the references to color in this figure legend, the reader is referred to the web version of this article.)

salinity appeared on the right side of the *Titli*'s track covering large area; however, on the left side, sea surface salinity increased mainly near the track.

3.3.3. Verification of different oceanic parameters during cyclone

Fig. 9 (a–g, shading) shows the estimated change (after minus before the passage of cyclone *Titli*) in SST (°C), sea surface salinity (psu), ILD (m), MLD (m), D26 (m), TCHP (Kjcm^{-2}) and ocean heat content (Kjcm^{-2}) from FIO-COM model. Anomalies in these parameters show the large-scale impact of *Titli* on the upper ocean of the northern bay. Argo observational data is used to compare the changes in these parameters from FIO-COM. Argo floats are available in seven positions in the vicinity of either side of the cyclone track of *Titli*. In the pre-cyclone period, Argo floats are available on 6 and 7 October and in the post-cyclone period, on the 11 and 12 of October. Therefore, 6 and 12 October are considered as pre-cyclone and post-cyclone period, respectively to obtain the anomalies in different parameters derived from Argo floats data.

The spatial distribution of the anomalies in different parameters from FIO-COM shows that the impact of cyclone *Titli* is larger on the right side of cyclone track. The maximum drop in SST by ~2.5 °C (Fig. 9a), maximum increase in sea surface salinity by ~1.0 psu (Fig. 9b), deepening in ILD and MLD by more than 20 m (Figs. 9c-d) from FIO-COM outputs. Moreover, shoaling of D26 by 15 m (Fig. 9e), decrease in ocean heat content by about 25 Kjcm^{-2} (Fig. 9f), and decrease in TCHP by about 15 Kjcm^{-2} (Fig. 9g) appear in model output. The strong winds on the right side of the cyclone track (contours of wind field overlaid in the Ekman pumping velocity field in Figs. 10 a1-c1) was observed during the cyclone days and the wind was the strongest in the very severe cyclone day (Fig. 10 b1). In general, the turbulence generated by the strongest winds would increase the vertical mixing (Maneesha et al., 2012). This cyclonic wind forcing along with the associated turbulent mixing on the right of the cyclone track generates inertial oscillation, which would facilitate the deeper and cooler mixed layer (Price, 1981) as observed in Fig. 9d.

Titli reduces the SST of the whole northern Bay of Bengal except the Andaman sea region (Fig. 9a). Spatial distribution of SST anomalies shows that reduction in SST occurs on either side of the cyclone track. However, decrease of SST on the right side of the cyclone track was about more than two times higher than that on the left side. The Argo floats also describe the similar spatial distribution of SST anomalies. Argo floats with ID 2902236, which is more northward from the cyclone track, showing SST cooling, and is well reproduced by the model (Fig. 9a and Table 2). Argo float on the left side of the cyclone track (ID 2902235) is showing reduction in SST although it is nearly three times lower than the float on the right side (ID 2902236). The strong winds (Fig. 10 a1-c1) and deepening of the MLD (Fig. 9d) associated with the cyclone *Titli* might help to reduce the SST (Kashem et al., 2019). Despite the fact that the increase in sea surface salinity did not cover the entire bay, the positive anomalous value covered a larger region on the right side of the cyclone track than it did on the left. Both model and Argo floats exhibit the similar distributions of sea surface salinity anomaly (Fig. 9b). Increase of sea surface salinity during post-cyclone period was due to strong vertical mixing.

Both ILD and MLD became deeper on both side of the cyclone track in the post-cyclone period, with the right side of the track being more extended (Figs. 9c, d). Both model simulation and Argo observational data give evidence for this phenomenon. Positive values of ILD and MLD anomalies after passing the area also observed in the region of cyclone generation (Figs. 9c, d; Table 2). In contrast to ILD and MLD, the cyclone *Titli* caused a shallowing of the depth of 26 °C isotherm along the cyclone track (Fig. 9e). Negative anomaly in D26 appeared from the very beginning days of the cyclone (Table 2). However, the shallowing of D26 was higher in the region of a very severe cyclonic storm days than in the zone of a low-intensity cyclone days. The heat content anomaly owing to cyclone has a similar pattern to the TCHP distribution, with the maximum heat loss occurring within the top 30 m depth and on days when cyclonic storms are very strong (Fig. 9f). The TCHP anomaly due to the cyclone *Titli* is displayed in Fig. 9g. The estimated change in TCHP along the track of cyclone *Titli* was negative with the highest loss of heat in the region of the highest drop of SST.

SST regulates the turbulent heat flux (latent and sensible heat fluxes), and warmer SST is a favorable environment for tropical cyclone genesis (Cione, 2015; Sun et al., 2019). Two-third of tropical cyclones form in the Northern Hemisphere with SST higher than 26 °C. Before generation of cyclone *Titli*, the SST was higher than 30 °C, which is shown both from model and Argo float at position (89.35°E, 13.45°N) (Fig. 9a). This remarkably high SST solely can intensify the tropical cyclone as observed in case of the tropical cyclones occurred on 26 April to 3 May 1994 (unnamed), 13 to 20 May 1997 (unnamed) and 24 to 29 April 2006 (named 'Mala') (Qiu et al., 2019). Before the generation of tropical cyclone *Titli*, ILD was also deeper (approximately 25.9 m), which is crucial for the intensification of a tropical cyclone, as 81% of the tropical cyclones intensifies under thick ILD condition (Qiu et al., 2019). Beside SST, the upper ocean thermal structure is also important for cyclone genesis and intensification. The available heat energy for the genesis and intensification of a cyclone can be estimated using TCHP. A strong storm can last a week with a TCHP of 33 Kjcm^{-2} and a temperature of 28 °C (Rao, 1986). Cyclone *Titli* generated with TCHP more than 75 Kjcm^{-2} (Table 2). Therefore, the tropical cyclone *Titli* was generated and intensified by both high SST and high TCHP, as well as deep ILD; and the effects of cyclone *Titli* was successfully reproduced by the FIO-COM.

3.3.4. Verification of upwelling features during cyclone

The wind during tropical cyclone strongly affects the upper ocean dynamics. The cyclonic wind stress induced divergence at surface causes Ekman transport (Ekman, 1905) radially away from the center of the cyclone. This Ekman transport causes upward Ekman pumping (Stommel, 1958), which results in cyclone-induced upwelling that shoals the thermocline and reduces SST (Jacob et al., 2000). The Ekman pumping velocity estimated from the GFS wind fields during the days of cyclone *Titli* is shown in Figs. 10 a1-c1. Positive value of Ekman pumping velocity indicates upwelling within the thermocline, whereas the negative Ekman pumping velocity specifies the downwelling of thermocline (Navaneeth et al., 2019). Significant positive values of Ekman pumping velocity were mostly confined along the cyclone track (Figs. 10 a1-c1). High Ekman pumping velocity was observed during the intense cyclone days. High Ekman pumping velocity (~5 × 10^{-4} ms^{-1}) along the cyclone track caused upwelling covering huge area on 11 October (Fig. 10 b1), which reduced the SST and increased sea surface salinity as observed in Fig. 11. The modeled vertical velocity is also highlighting the cyclone-induced upwelling features along the cyclone track during these cyclone days (Figs. 10 a2-c2).

Fig. 11 (a1, b1) depicts the vertical section of temperature and salinity in the Bay of Bengal during the very severe cyclonic passage on October 11 spanning longitude 85.85°E with latitudes ranging from 14.9 to 19.0°N from FIO-COM analysis output. Both temperature and salinity profiles along the 17°N latitudes show clear signs of cyclone-induced upwelling. In comparison to other latitudes, the vertical temperature contours exhibit a concave up form towards the sea surface (SST >28.5 °C) in 17.3–17.7°N latitudes, where tropical cyclone *Titli* induced upwelling has contributed 2–2.5 °C cooling over the sea surface (Fig. 11 a1). Notably, about 70–80% of SST cooling during tropical cyclone results from vertical processes due to tropical cyclone-induced upwelling (Price, 1981; Vincent et al., 2012a, 2012b). The thermocline was also shoaled at the locations of 17.3°N to 17.7°N latitudes after the passage of cyclone *Titli* (Fig. 11 a1). Cooling of the SST in the region is also evident from the surface plot derived from the SST data of MW_IR (Fig. 11 a2). Similar to the vertical section of temperature, a band of high saline (>33.5 PSU) waters exhibits within the upper 60 m depths and enhances the sea surface salinity by 1.0–1.5 psu in FIO-COM outputs in

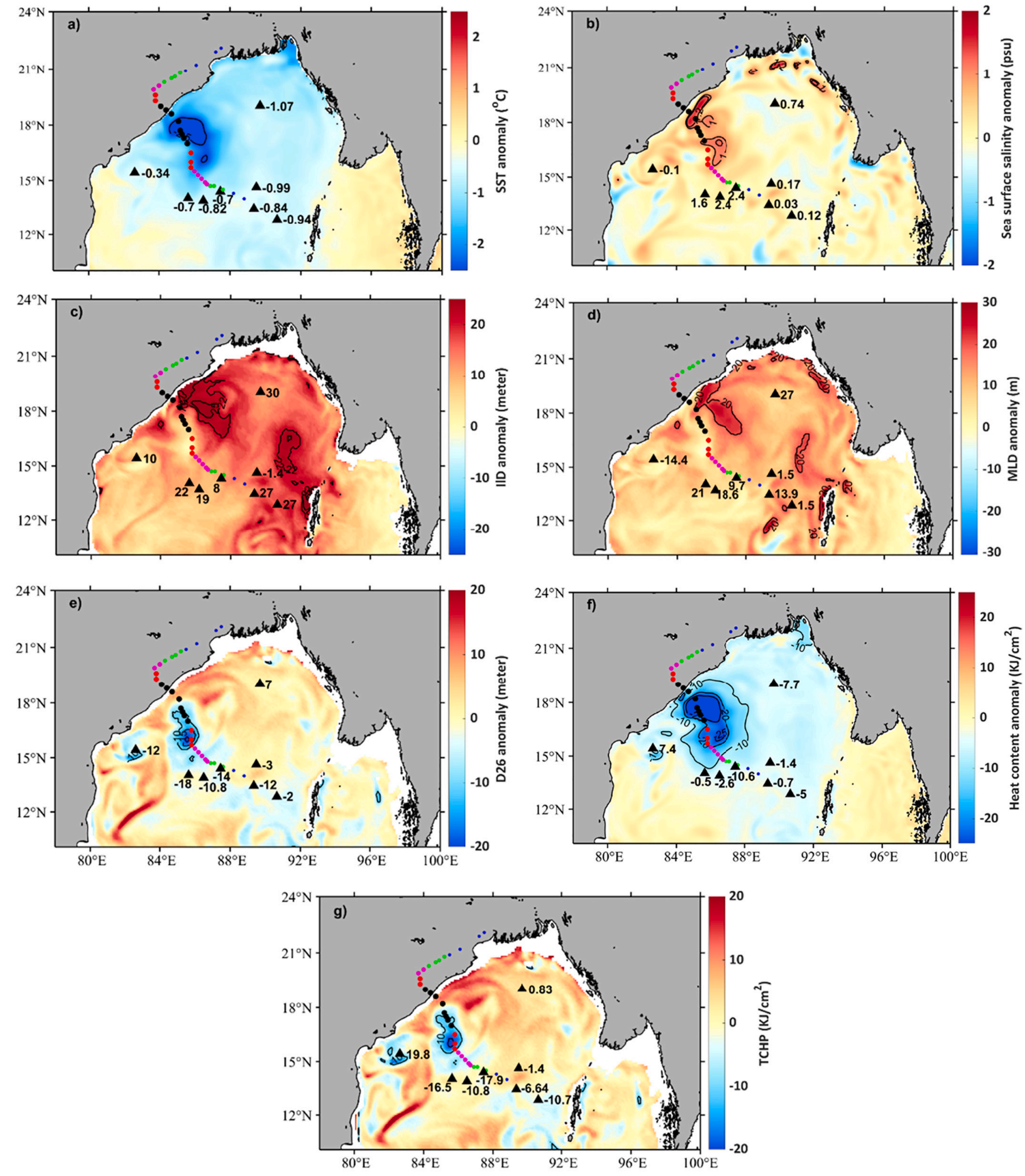

Fig. 9. Estimated SST anomaly (°C) (a), sea surface salinity (psu) (b), ILD (m) (c), MLD (m) (d), depth of 26 °C isotherm (D26) (m) (e), heat content (Kjcm^{-2}) (f), and TCHP (Kjcm^{-2}) (g) before (6 October) and after (12 October) the cyclone '*Titli*' from FIO-COM outputs. Small black filled upper triangles indicate the Argo floats position with ID as described in Fig. 1b and the values in text are the anomaly of the respective parameters after (12 October) and before (6 October) for the cyclone *Titli*.

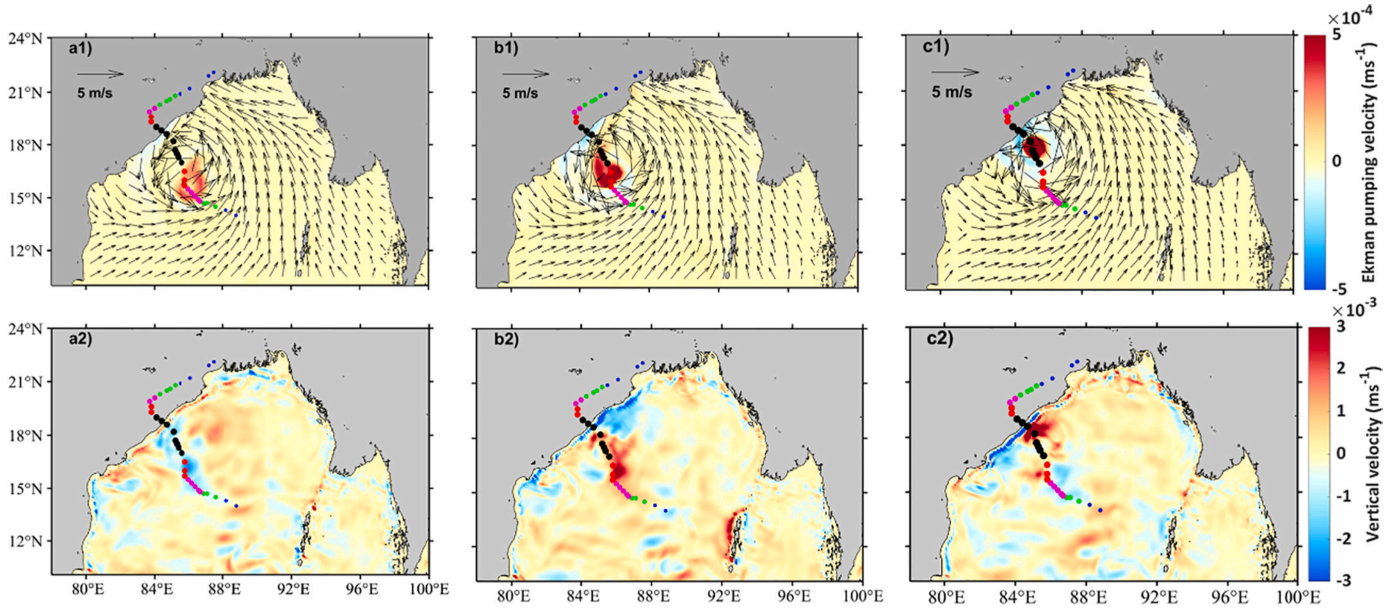

Fig. 10. Ekman pumping velocity (ms^{-1}) overlaid with the wind vector during the intense cyclone days and the modeled vertical velocity on 10 October (a1, a2), 11 October (b1, b2), and 12 October (c1, c2), respectively. Modeled vertical velocity is averaged within upper 50-m depth of the ocean.

Table 2
Values of different parameters before cyclone in the Argo floats positions and anomalies of parameters before and after cyclone from Argo profiles and FIO-COM.

Argo ID	Position (lon, lat)	SST (°C)		SSS (psu)		MLD (m)		ILD (m)		D26 (m)		TCHP (KJ/cm^2)		HC (KJ/cm^2)	
Model		BC	AY	BC	AY	BC	AY	BC	AY	BC	AY	BC	AY	BC	AY
2,902,236	89.7°E,	30.2	−1.07	31.5	0.74	12.9	27	25	30	60	7	73.54	0.83	498.6	−7.7
FIO-COM	19.03°N	30.1	−0.51	32.7	−0.21	26.2	5.7	29	9	57	1	63.08	3.15	502.1	−5
2,902,235	90.7°E,	29.7	−0.94	32.4	0.12	16.4	1.5	23	27	62	−2	60.46	−10.7	488.5	−5
FIO-COM	12.9°N	29.6	−0.3	33.3	−0.1	43.4	1.1	47	3	75	−3	84.54	−2.49	497.6	−4.08
2,902,232	89.4°E, 13.5°N	30.3	−0.85	33	0.03	11.1	14	13	27	67	−12	68.44	−6.64	492.4	−0.7
FIO-COM		29.6	−0.29	33.5	0.22	37.5	2.2	44	1	70	0	78.29	1.32	496.6	−2.8
2,902,234	86.5°E, 13.9°N	30.2	−0.82	31	2.4	8.1	18.6	19	19	44	−10	48.6	−10.9	492.7	−2.6
FIO-COM		29.8	−0.48	32.3	0.2	21.5	5.7	27	6	52	−2	57.5	−0.04	496.5	−4.9
2,902,233	85.6°E, 14.04°N	30.4	−0.7	31.2	1.6	7.6	21	16	22	56	−18	67.9	−16.5	498.4	−0.5
FIO-COM		29.9	−0.7	32.2	0.1	20.3	7.5	27	7	51	−1	56.4	1.1	497.9	−6.7
6,901,740	82.6°E, 15.43°N	30.1	−0.34	31.7	−0.1	4.5	−14.4	9	10	61	−12	65.1	19.8	498.9	7.4
FIO-COM		30.2	−0.49	31.7	0.13	19.2	3.3	22	4	43	−4	48.89	−5.54	498.3	−3.7
2,902,264	87.5°E, 14.4°N	30.1	−1.24	32.4	2.4	20.1	9.7	21	8	27	−14	39.13	−17.9	489.6	−10.6
FIO-COM		30	−0.57	32.5	0.02	22.1	6.5	30	8	57	−1	63.08	0.97	496.1	−6.1

Note: lon is longitude, lat is latitude, SSS is sea surface salinity, HC is heat content, BC is before cyclone and AY is anomaly.

17.3–17.7°N latitudes as compared to either southern or northern latitudinal regions (Fig. 11 b1). This elevated salinity like upwelling feature is also observed from the SMAP sea surface salinity in the region on the same day of cyclone (Fig. 11 b2).

Fig. 12 demonstrates the predicted change in SST (averaged over the rectangular box shown in Fig. 1a) due to cyclone *Titli* derived from the FIO-COM results of respective analysis and forecasting days. Decrease in SST due to upwelling during cyclone is also evident from this figure, which demonstrates that the model predicted the SST during cyclone well. Both the analysis and forecasted output of the model shows that at the very beginning of the cyclone days SST was higher, during cyclone SST reduced and after the cyclone SST also remained lower than the earlier days of cyclone. This variation of SST due to cyclone *Titli* is also observed from the MW_IR data. Although the SST were predicted with good accuracy at the early stages of cyclone generation and after landfall, performance was slightly reduced during cyclone.

4. Conclusions

The performance of the high-resolution (~10 km) global model FIO-COM is validated in the northern Bay of Bengal (10°-23°N, 80°-100°E). RAMA buoys, Argo profiles, EN4 observational profiles, and satellite datasets are utilized to assess the performance of FIO-COM analysis data and forecasting outputs. The validation is carried out through: (1) examining the seasonal variations of temperature and salinity (spatial distributions and vertical profiles) obtained from the model analysis data; (2) quantitatively assessing the daily SST, sea surface salinity, ILD, MLD, BLT, D26, TCHP, and ocean heat content with the observational data from RAMA buoys at positions (15°N, 90°E) and (12°N, 90°E); and (3) examining the performance of FIO-COM in capturing the changes in the upper ocean thermodynamics during tropical cyclone *Titli* as well as predicting the SST on succeeding days.

SST and vertical profiles of temperature from FIO-COM accurately reproduces the seasonal pattern of temperature across the northern Bay of Bengal. In comparison to prior research (RMSE up to 1 °C), SST from FIO-COM corresponds well with EN4 data, with SST RMSE 0.47 to 0.71 °C. The vertical temperature profiles at three distinct places in the bay (northern, eastern, and western points) also correspond well with EN4 data, with much smaller RMSE (about 0.27 to 1.0 °C) than prior studies (RMSE 1.0 to 2.3 °C), and our model has represented the

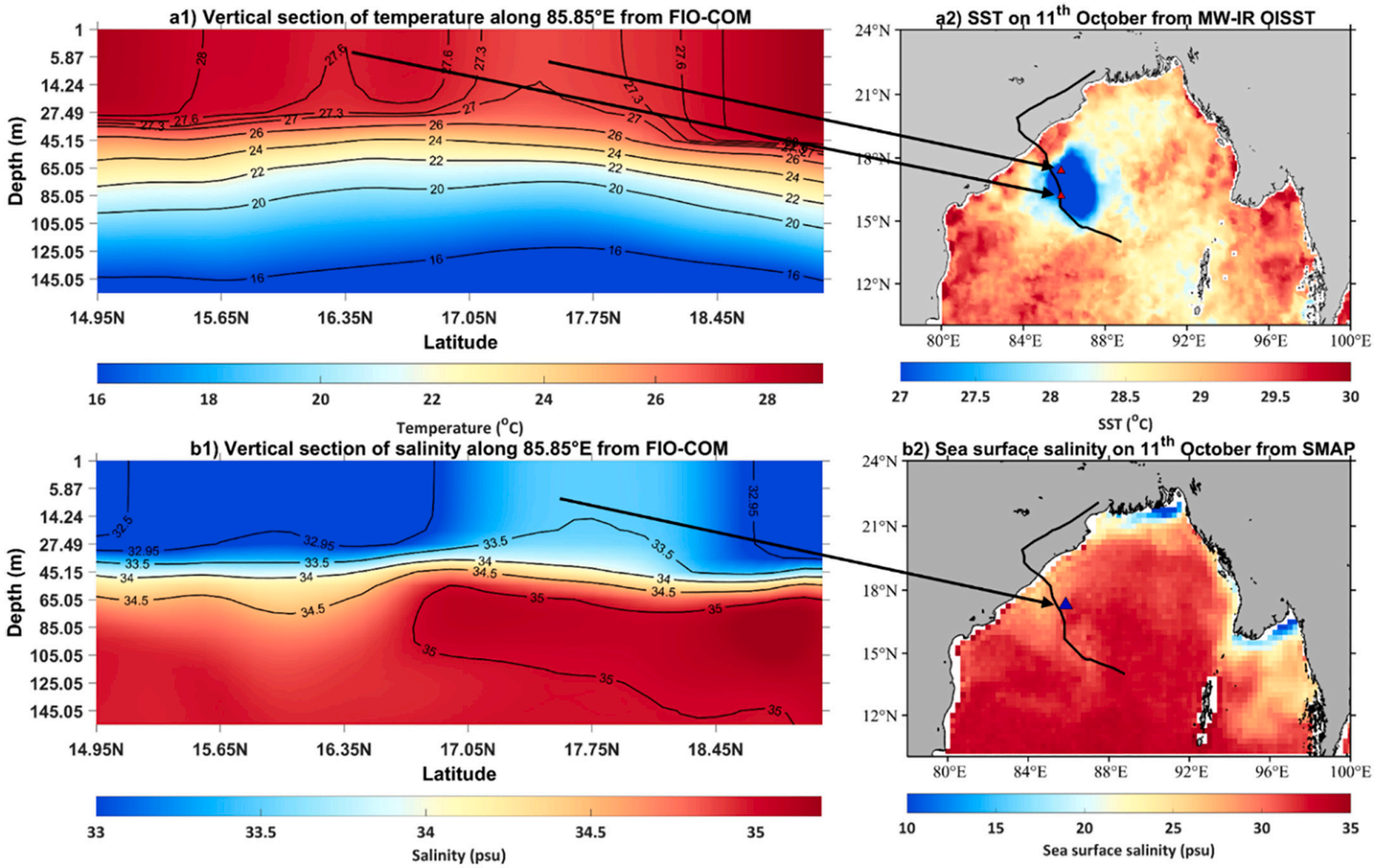

Fig. 11. Vertical sections of temperature (°C) (upper-left panel) (a1), and salinity (psu) (lower-left panel) (b1), along 85.85°E longitude show the upwelling feature in model. SST (°C) from MW_IR (a2), and sea surface salinity (psu) from SMAP (b2) also exhibit the signature of upwelling as pointed by upper triangles with filled red and blue color, respectively. (For interpretation of the references to color in this figure legend, the reader is referred to the web version of this article.)

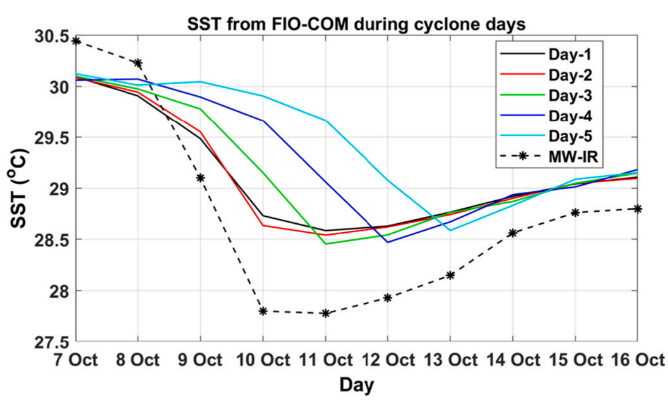

Fig. 12. Four days forecast by the FIO-COM model along with the SST (°C) on analysis day both from FIO-COM and MW_IR daily data.

thermocline remarkably well. Inclusion of the non-breaking surface wave-induced mixing in FIO-COM is favoring for this realistic thermocline results. The model, like EN4 data, can accurately describe the commencement and expansion of freshwater routes, especially monsoonal freshwater flow along the eastern and western coasts. The FIO-COM's output has accurately represented seasonal variations in surface and vertical structure of salinity with RMSE 0.62 to 0.83 psu, compared with a previously reported bigger bias (1.5 psu). The bias in salinity profiles is the highest at the northernmost RAMA buoy point (RMSE 0.22 to 0.56 psu), where huge freshwater come from adjacent rivers compared with the other points (RMSE 0.11 to 0.38 psu).

Daily variations in different oceanic parameters including SST, sea surface salinity, ILD, MLD, BLT, D26, TCHP, and ocean heat content at positions (15°N, 90°E) and (12°N, 90°E) are well captured by FIO-COM analysis, which is comparable with those of the RAMA buoy data. FIO-COM also provides reasonable accuracy to predict the above-mentioned parameters on leading days. FIO-COM obtains more accurate results especially the MLD and TCHP in this area because of the non-breaking wave-induced mixing. However, RMSE from the analyses and prediction of ILD, MLD, BLT, and other salinity associated parameters is comparatively higher at the northern most RAMA buoy (15°N, 90°E), and comparatively lower error is found in southern part of the bay, where influence of river discharge is less. The biasness in salinity can be reduced by the inclusion of more regional rivers in the model.

Performance of the FIO-COM model in capturing the response of the upper ocean thermohaline structure to the passage of tropical cyclone *Titli* is validated. Generally, FIO-COM outputs are in good agreement with the MW_IR and SMAP data during and after this cyclone in capturing the change in SST and sea surface salinity, respectively. Both model and remote sensing data show pronounced SST cooling (approximately 2.0–2.5 °C) and increased sea surface salinity (~ 1 psu) on the right side of the cyclone track during 10 to 12 October of 2018. FIO-COM outputs are in good agreement with the observational Argo floats to capture the variations in ILD, MLD, D26, TCHP, and heat content. High SST (>30 °C) and deep ILD were the main oceanic triggering forces to intensify the cyclone *Titli*, according to both FIO-COM and Argo floats data. During initial stages of cyclone, TCHP was high (more than 75 Kjcm^{-2}), which was also responsible to enhance a depression into a very severe cyclonic storm. High positive Ekman pumping velocity generated upwelling was simulated from FIO-COM data. Upwelling caused the uplifting of isotherms (reduction in SST by 2.0 to 2.5 °C) and isohalines (increased in sea surface salinity by 1.0 to 1.5 psu) along the 85.85°E longitudes in the northern Bay of Bengal, which were also observed from the spatial distribution of the SST and sea surface salinity from satellite data. Just at the beginning and land fall time of the cyclone, SST was predicted with excellent accuracy from the FIO-COM. With the increase in lead time, FIO-COM's predicting accuracy decreased slightly, which is a well-known characteristic of all OFS systems.

FIO-COM model forcing, initial and boundary conditions, and the non-breaking surface wave-induced mixing could be carefully considered in future attempts to establish a regional OFS, because FIO-COM captured the cyclonic response and also the seasonal thermohaline dynamics in the upper northern Bay of Bengal quite well. However, more groundwork should be done to identify the appropriate atmospheric forcing and model physics in this bay. Moreover, future regional OFS initiatives should include more realistic freshwater sources.

CRediT authorship contribution statement

Shaila Akhter: Conceptualization; Data curation; Formal analysis, Software, Writing - original draft & Editing.

Fangli Qiao: Supervision, Writing review & Funding acquisition.

Kejian Wu: Supervision, Editing, revised manuscript critically for important intellectual content.

Xunqiang Yin: acquisition, analysis, or interpretation of data, review.

K M Azam Chowdhury: Investigation, made substantial contributions to the conception and design of the work.

Md. Kawser Ahmed: Supervision, review.

A. S. M. Maksud Kamal: Supervision, review.

Declaration of Competing Interest

The authors declare that they have no known competing financial interests or personal relationships that might have appeared to influence the work reported in this research paper.

Acknowledgements

Authors are grateful to EN4, Argo, and RAMA for their data. The gratitude is extended to the Chinese Scholarship Council for offering scholarship, which facilitates to do this research. In addition, authors are thankful to the First Institute of Oceanography, Ministry of Natural Resources of China for their all kind of supports. This research is supported by the National Natural Science Foundation of China under grant 41821004.

References

Akhil, V.P., Durand, F., Lengaigne, M., Vialard, J., Keerthi, M.G., Gopalakrishna, V.V., Deltel, C., Papa, F., de Boyer, Montégut C., 2014. A modeling study of the processes of surface salinity seasonal cycle in the Bay of Bengal. J. Geophys Res. Oceans 119 (6), 3926–3947. https://doi.org/10.1002/2013JC009632.

Akhter, S., Qiao, F., Wu, K., Yin, X., Chowdhury, K.A., Chowdhury, N.U.M.K., 2021. Seasonal and long-term sea-level variations and their forcing factors in the northern Bay of Bengal: a statistical analysis of temperature, salinity, wind stress curl, and regional climate index data. Dyn. Atmos. Oceans 95, 101239. https://doi.org/10.1016/j.dynatmoce.2021.101239.

Allison, M.A., 1998. Historical changes in the Ganges-Brahmaputra delta front. J. Coast. Res. 14 (4), 1269–1275.

Anonymous, 1979. Tracks of Storms and Depressions in the Bay of Bengal and the Arabian Sea 1877–1970. India Meteorological Department, New Delhi.

Argo, 2000. Argo Float Data and Metadata from Global Data Assembly Centre (Argo GDAC). SEANOE. https://doi.org/10.17882/42182. Accessed 1 September 2021.

Behara, A., Vinayachandran, P.N., 2016. An OGCM study of the impact of rain and river water forcing on the Bay of Bengal. J. Geophys Res. Oceans 121 (4), 2425–2446. https://doi.org/10.1002/2015JC011325.

Bender, M.A., Ginis, I., Kurihara, Y., 1993. Numerical simulations of tropical cyclone-ocean interaction with a high-resolution coupled model. J. Geophys. Res. Atmos. 98 (D12), 23245–23263. https://doi.org/10.1029/93JD02370.

Berg, R., 2002. Tropical cyclone intensity in relation to SST and moisture variability: A global perspective. In: Proceedings of the 25th Conference on Hurricanes and Tropical Meteorology. American Meteorological Society, San Diego, CA, USA, 29 April–3 May 2002.

Black, W.J., Dickey, T.D., 2008. Observations and analyses of upper ocean responses to tropical storms and hurricanes in the vicinity of Bermuda. J. Geophys Res. Oceans 113 (C8), C08009. https://doi.org/10.1029/2007JC004358.

Boyer, T.P., Antonov, J.I., Baranova, O.K., Coleman, C., Garcia, H.E., Grodsky, A., Johnson, D.R., Locarnini, R.A., Mishonov, A.V., O'Brien, T.D., Zweng, M.M., 2013. World Ocean Database 2013. In: Levitus, S. (Ed.), NOAA Atlas NESDIS 72. National Oceanographic Data Center, Silver Spring, MD, p. 208.

Brassington, G.B., Pugh, T., Spillman, C., Schulz, E., Beggs, H., Schiller, A., Oke, P.R., 2007. BLUElink> development of operational oceanography and servicing in Australia. J. Res. Pract. Inf. Technol. 39 (2), 151–164.

Chaitanya, A.V.S., Lengaigne, M., Vialard, J., Gopalakrishna, V.V., Durand, F., Kranthikumar, C., Amritash, S., Suneel, V., Papa, F., Ravichandran, M., 2014. Salinity measurements collected by fishermen reveal a "river in the sea" flowing along the eastern coast of India. Bull. Am. Meteorol. Soc. 95 (12), 1897–1908. https://doi.org/10.1175/BAMS-D-12-00243.1.

Chakraborty, A., Gangopadhyay, A., 2016a. Development of a high-resolution multiscale modeling and prediction system for Bay of Bengal, part I: climatology-based simulations. Open J. Mar. Sci. 6 (1), 145–176. https://doi.org/10.4236/ojms.2016.61013.

Chakraborty, A., Gangopadhyay, A., 2016b. Development of a high-resolution multiscale modeling and prediction system for Bay of Bengal, part II: an application to October 2008. Open J. Mar. Sci. 6 (01), 125–144. https://doi.org/10.4236/ojms.2016.61012.

Chen, G., Wang, X., 2016. Vertical structure of upper-ocean seasonality: annual and semiannual cycles with oceanographic implications. J. Clim. 29 (1), 37–59. https://doi.org/10.1175/JCLI-D-14-00855.1.

Chinthalu, G.R., Seetaramayya, P., Ravichandran, M., Mahajan, P.N., 2001. Response of the Bay of Bengal to Gopalpur and Paradip super cyclones during 15–31 October 1999. Curr. Sci. 81 (3), 283–291.

Chowdhury, K.M.A., Jiang, W.S., Liu, G.M., Ahmed, M.K., Akhter, S., 2021a. Spatiotemporal variation and mechanisms of temperature inversion in the Bay of Bengal and eastern equatorial Indian Ocean. Acta Oceanol Sin (accepted on 11 June 2021).

Chowdhury, K.M.A., Jiang, W.S., Liu, G.M., Ahmed, M.K., Akhter, S., 2021b. Dominant physical-biogeochemical drivers for seasonal variations in surface chlorophyll-a and subsurface chlorophyll-a maximum in the Bay of Bengal. Reg. Stud. Mar. Sci. 48, 102022 (accepted on 25 September 2021).

Cione, J.J., 2015. The relative roles of the ocean and atmosphere as revealed by buoy air–sea observations in hurricanes. Mon. Weather Rev. 143 (3), 904–913. https://doi.org/10.1175/MWR-D-13-00380.1.

Cione, J.J., Uhlhorn, E.W., 2003. Sea surface temperature variability in hurricanes: implications with respect to intensity change. Mon. Weather Rev. 131 (8), 1783–1796. https://doi.org/10.1175//2562.1.

de Boyer Montégut, C, Madec, G, Fischer, AS, Lazar, A, Iudicone, D, 2004. Mixed layer depth over the global ocean: An examination of profile data and a profile-based climatology. 109(C12) https://doi.org/10.1029/2004JC002378.

de Boyer Montégut, C, Vialard, J, Shenoi, S.S.C., Shankar, D, Durand, F, Ethé, C, et al., 2007. Simulated seasonal and interannual variability of mixed layer heat budget in the northern Indian Ocean 20, 3249–3268.

Ekman, V.W., 1905. On the influence of the earth's rotation on ocean-currents. Arkiv Matematik Astronomi Och Fysik 2 (11), 1–52.

Ezer, T., 2000. On the seasonal mixed layer simulated by a basin-scale ocean model and the Mellor-Yamada turbulence scheme. J. Geophys Res. Oceans 105 (C7), 16843–16855. https://doi.org/10.1029/2000JC900088.

Fathrio, I., Manda, A., Iizuka, S., Kodama, Y.M., Ishida, S., 2017. Evaluation of CMIP5 models on sea surface salinity in the Indian Ocean. IOP Conf. Ser. Earth Environ. Sci. 54, 012039 https://doi.org/10.1088/1755-1315/54/1/012039.

Felton, C.S., Subrahmanyam, B., Murty, V.S.N., Shriver, J.F., 2014. Estimation of the barrier layer thickness in the Indian Ocean using Aquarius Salinity. J. Geophys Res. Oceans 119 (7), 4200–4213. https://doi.org/10.1002/2013JC009759.

Foltz, G.R., Grodsky, S.A., Carton, J.A., McPhaden, M.J., 2003. Seasonal mixed layer heat budget of the tropical Atlantic Ocean. J. Geophys Res. Oceans 108 (C5), 3146. https://doi.org/10.1029/2002JC001584.

Francis, P.A., Vinayachandran, P.N., Shenoi, S.S.C., 2013. The Indian Ocean forecast system. Curr. Sci. 104 (10), 1354–1368.

Francis, P.A., Jithin, A.K., Effy, J.B., Chatterjee, A., Chakraborty, K., Paul, A., Balaji, B., Shenoi, S.S.C., Biswamoy, P., Mukherjee, A., Satyanarayana, B.V., 2020. High-resolution operational ocean forecast and reanalysis system for the Indian ocean. Bull. Am. Meteorol. Soc. 101 (8), E1340–E1356. https://doi.org/10.1175/BAMS-D-19-0083.1.

Girishkumar, M.S., Ravichandran, M., Han, W., 2013. Observed intraseasonal thermocline variability in the Bay of Bengal. J. Geophys Res. Oceans 118 (7), 3336–3349. https://doi.org/10.1002/jgrc.20245.

Goni, G., DeMaria, M., Knaff, J., Sampson, C., Ginis, I., Bringas, F., Mavume, A., Lauer, C., Lin, I.I., Ali, M.M., Halliwell, G., 2009. Applications of satellite-derived ocean measurements to tropical cyclone intensity forecasting. Oceanogr 22 (3), 190–197.

Good, S.A., Martin, M.J., Rayner, N.A., 2013. EN4: Quality controlled ocean temperature and salinity profiles and monthly objective analyses with uncertainty estimates. J. Geophys Res. Oceans 118 (12), 6704–6716. https://doi.org/10.1002/2013JC009067.

Gopalakrishna, V.V., Murty, V.S.N., Sarma, M.S.S., Sastry, J.S., 1993. Thermal response of upper layers of bay of Bengal to forcing of a severe cyclonic storm: a case study. Indian J. Mar. Sci. 22, 8–11.

Gouretski, V., Reseghetti, F., 2010. On depth and temperature biases in bathythermograph data: development of a new correction scheme based on analysis of a global ocean database. Deep Sea Res. I Oceanogra Res. Pap. 57 (6), 812–833. https://doi.org/10.1016/j.dsr.2010.03.011.

Griffies, S.M., 2012. Elements of the modular ocean model (MOM) (2012 release with updates), GFDL ocean group technical report No. 7, NOAA/Geophysical Fluid Dynamics Laboratory, p. 632 + xiii.

He, S., Peng, Y., Jin, Y., Wan, B., 2020. Research on design and pressure-retaining performance of the pressure-retaining sampler for full-ocean-depth sediment. Int. J. Mater. Prod. Technol. 60 (2–4), 161–179. https://doi.org/10.1504/IJMPT.2020.110116.

Howden, S.D., Murtugudde, R., 2001. Effects of river inputs into the bay of Bengal. J. Geophys Res. Oceans 106 (C9), 19825–19843. https://doi.org/10.1029/2000JC000656.

Huang, C.J., Qiao, F., 2010. Wave-turbulence interaction and its induced mixing in the upper ocean. J. Geophys Res. Oceans 115 (C4), C04026. https://doi.org/10.1029/2009JC005853.

Huang, C.J., Qiao, F., Song, Z., Ezer, T., 2011. Improving simulations of the upper ocean by inclusion of surface waves in the Mellor-Yamada turbulence scheme. J. Geophys Res. Oceans 116 (C1), C01007. https://doi.org/10.1029/2010JC006320.

Hurlburt, H.E., Drillet, Y., Brassington, G.B., Benkiran, M., Chassignet, E.P., Cummings, J.A., Drevillon, M., Etienne, H., Galloudec, O.L., Metzger, E.J., Warren, G., 2008. Global high-resolution analyses and forecasts at the mesoscale. In: Conference Proceedings Final GODAE Symposium, November 12–15, 2008, pp. 95–111. Nice, France.

IMD, 2018. Very Severe Cyclonic Storm "TITLI" over Bay of Bengal (07–13 Oct. 2018) and Very Severe Cyclonic Storm "LUBAN" over Arabian Sea (06–14 October 2018). India Meteorological Department. https://reliefweb.int/sites/reliefweb.int/files/resources/20181016_pr_347.pdf.

Jacob, S.D., Shay, L.K., Mariano, A.J., Black, P.G., 2000. The 3D oceanic mixed layer response to hurricane Gilbert. J. Phys. Oceanogr. 30 (6), 1407–1429. https://doi.org/10.1175/1520-0485(2000)030%3C1407:TOMLRT%3E2.0.CO;2.

Jana, S., Gangopadhyay, A., Chakraborty, A., 2015. Impact of seasonal river input on the Bay of Bengal simulation. Cont. Shelf Res. 104, 45–62. https://doi.org/10.1016/j.csr.2015.05.001.

Jana, S., Gangopadhyay, A., Lermusiaux, P.F., Chakraborty, A., Sil, S., Haley Jr., P.J., 2018. Sensitivity of the Bay of Bengal upper ocean to different winds and river input conditions. J. Mar. Syst. 187, 206–222. https://doi.org/10.1016/j.jmarsys.2018.08.001.

Jensen, T.G., Wijesekera, H.W., Nyadjro, E.S., Thoppil, P.G., Shriver, J.F., Sandeep, K.K., Pant, V., 2016. Modeling salinity exchanges between the equatorial Indian Ocean and the Bay of Bengal. Oceanogr 29 (2), 92–101.

Ji, Q., Zhu, X., Wang, H., Liu, G., Gao, S., Ji, X., Xu, Q., 2015. Assimilating operational SST and sea ice analysis data into an operational circulation model for the coastal seas of China. Acta Oceanol. Sin. 34 (7), 54–64. https://doi.org/10.1007/s13131-015-0691-y.

Kara, A.B., Rochford, P.A., Hurlburt, H.E., 2000. An optimal definition for ocean mixed layer depth. J. Geophys Res. Oceans 105 (C7), 16803–16821. https://doi.org/10.1029/2000JC900072.

Kashem, M., Ahmed, M.K., Qiao, F., Akhter, M.A.E., Chowdhury, K.M.A., 2019. The response of the upper ocean to tropical cyclone Viyaru over the bay of Bengal. Acta Oceanol. Sin. 38 (1), 61–70. https://doi.org/10.1007/s13131-019-1370-1.

Kourafalou, V.H., De Mey, P., Le Hénaff, M., Charria, G., Edwards, C.A., He, R., Herzfeld, M., Pascual, A., Stanev, E.V., Tintoré, J., Zhu, X., 2015. Coastal Ocean forecasting: system integration and evaluation. J Oper Oceanogr 8 (sup1), s127–s146. https://doi.org/10.1080/1755876X.2015.1022336.

Kumari, A., Kumar, S.P., Chakraborty, A., 2018. Seasonal and interannual variability in the barrier layer of the Bay of Bengal. J. Geophys Res. Oceans 123 (2), 1001–1015. https://doi.org/10.1002/2017JC013213.

Lee, S.K., Park, W., Baringer, M.O., Gordon, A.L., Huber, B., Liu, Y., 2015. Pacific origin of the abrupt increase in Indian Ocean heat content during the warming hiatus. Nat. Geosci. 8 (6), 445–449. https://doi.org/10.1038/ngeo2438.

Levitus, S., Antonov, J.I., Boyer, T.P., Locarnini, R.A., Garcia, H.E., Mishonov, A.V., 2009. Global Ocean heat content 1955–2008 in light of recently revealed instrumentation problems. Geophys. Res. Lett. 36 (7), L07608. https://doi.org/10.1029/2008GL037155.

Li, K., Wang, H., Yang, Y., Yu, W., Li, L., 2016. Observed characteristics and mechanisms of temperature inversion in the northern Bay of Bengal. Haiyang Xuebao 38 (7), 22–31.

Mahapatra, D.K., Rao, A.D., Babu, S.V., Srinivas, C., 2007. Influence of coast line on upper ocean's response to the tropical cyclone. Geophys. Res. Lett. 34 (17), L17603. https://doi.org/10.1029/2007GL030410.

Maneesha, K., Murty, V.S.N., Ravichandran, M., Lee, T., Yu, W., McPhaden, M.J., 2012. Upper Ocean variability in the Bay of Bengal during the tropical cyclones Nargis and Laila. Prog. Oceanogr. 106, 49–61. https://doi.org/10.1016/j.pocean.2012.06.006.

Masson, S., Delecluse, P., Boulanger, J.P., Menkes, C., 2002. A model study of the seasonal variability and formation mechanisms of the barrier layer in the eastern equatorial Indian Ocean. J. Geophys Res. Oceans 107 (C12). https://doi.org/10.1029/2001JC000832. SRF-18.

Masud-Ul-Alam, Md, Khan, MdAI, Barrett, B.S., Rivero-Calle, S., 2022. Surface temperature and salinity in the northern bay of Bengal: in situ measurements compared with satellite observations and model output. J. Appl. Remote. Sens. 16 (1) https://doi.org/10.1117/1.JRS.16.018502.

McCreary, J.P., Han, W., Shankar, D., Shetye, S.R., 1996. Dynamics of the east India coastal current: 2. Numerical solutions. J. Geophys Res. Oceans 101 (C6), 13993–14010. https://doi.org/10.1029/96JC00560.

McPhaden, M.J., Foltz, G.R., Lee, T., Murty, V.S.N., Ravichandran, M., Vecchi, G.A., Vialard, J., Wiggert, J.D., Yu, L., 2009a. Ocean-atmosphere interactions during cyclone nargis. EOS Trans. Am. Geophys. Union 90 (7), 53–54. https://doi.org/10.1029/2009EO070001.

McPhaden, M.J., Meyers, G., Ando, K., Masumoto, Y., Murty, V.S.N., Ravichandran, M., Syamsudin, F., Vialard, J., Yu, L., Yu, W., 2009b. RAMA: the research moored array for African–Asian–Australian monsoon analysis and prediction. Bull. Am. Meteorol. Soc. 90 (4), 459–480. https://doi.org/10.1175/2008BAMS2608.1.

Mehra, A., Rivin, I., 2010. A real time ocean forecast system for the North Atlantic Ocean. Terr. Atmos. Ocean. Sci. 21 (1), 211–228. https://doi.org/10.3319/TAO.2009.04.16.01(IWNOP).

Mellor, G., 2003. The three-dimensional current and surface wave equations. J. Phys. Oceanogr. 33 (9), 1978–1989. https://doi.org/10.1175/1520-0485(2003)033%3C1978:TTCASW%3E2.0.CO;2.

MoFA, 2014. Press Release: Press Statement of the Hon'ble Foreign Minister on the Verdict of the Arbitral Tribunal/PCA. Ministry of Foreign Affairs, Bangladesh. http://www.mofa.gov.bd/PressRelease/PRDetails.php?txtUserId=&PRid=854. Accessed 1 September 2021.

Murty, V.S.N., Sarma, M.S.S., Tilvi, V., 2000. Seasonal cyclogenesis and the role of near-surface stratified layer in the Bay of Bengal. In: Fifth Pacific Ocean Remote Sensing Conference, PORSEC, Vol. I, NIO, Goa, India during 5–8 December, 2000, pp. 453–457.

Narvekar, J., Prasanna Kumar, S., 2014. Mixed layer variability and chlorophyll a biomass in the Bay of Bengal. Biogeosciences 11 (14), 3819–3843. https://doi.org/10.5194/bg-11-3819-2014.

Navaneeth, K.N., Martin, M.V., Joseph, K.J., Venkatesan, R., 2019. Contrasting the upper ocean response to two intense cyclones in the bay of Bengal. Deep Sea Res. I Oceanogr. Res. Pap. 147, 65–78. https://doi.org/10.1016/j.dsr.2019.03.010.

Obasi, G.O.P., 1997. WMO's programme on tropical cyclone. Mausam 48 (2), 103–112.

Palmen, E., 1948. On the formation and structure of tropical hurricanes. Geophys 3 (1), 26–38.

Pant, V., Girishkumar, M.S., Udaya Bhaskar, T.V.S., Ravichandran, M., Papa, F., Thangaprakash, V.P., 2015. Observed interannual variability of near-surface salinity in the Bay of Bengal. J. Geophys Res. Oceans 120 (5), 3315–3329. https://doi.org/10.1002/2014JC010340.

Papa, F., Bala, S.K., Pandey, R.K., Durand, F., Gopalakrishna, V.V., Rahman, A., Rossow, W.B., 2012. Ganga-Brahmaputra River discharge from Jason-2 radar altimetry: an update to the long-term satellite-derived estimates of continental freshwater forcing flux into the bay of Bengal. J. Geophys Res. Oceans 117 (C11), C11021. https://doi.org/10.1029/2012JC008158.

Price, J.F., 1981. Upper Ocean response to a hurricane. J. Phys. Oceanogr. 11 (2), 153–175. https://doi.org/10.1175/1520-0485(1981)011%3C0153:UORTAH%3E2.0.CO;2.

Qiao, F., Yuan, Y., Yang, Y., Zheng, Q., Xia, C., Ma, J., 2004. Wave-induced mixing in the upper ocean: distribution and application to a global ocean circulation model. Geophys. Res. Lett. 31 (11), L11303. https://doi.org/10.1029/2004GL019824.

Qiao, F., Yang, Y., Xia, C., 2008. The role of surface waves in the ocean mixed layer. Acta Oceanol. Sin. 27 (3), 30–37.

Qiao, F., Yuan, Y., Ezer, T., Xia, C., Yang, Y., Lü, X., Song, Z., 2010. A three-dimensional surface wave–ocean circulation coupled model and its initial testing. Ocean Dyn. 60 (5), 1339–1355. https://doi.org/10.1007/s10236-010-0326-y.

Qiao, F., Zhao, W., Yin, X., Huang, X., Liu, X., Shu, Q., et al., 2016a. A highly effective global surface wave numerical simulation with ultra-high resolution. In: Proceedings of the International Conference for High Performance Computing, Networking, Storage and Analysis (SC16). IEEE Press, Piscataway, NJ, ISBN 978-1-4673-8815-3, pp. 46–56. Article 5. Retrieved From. http://dl.acm.org/citation.cfm?id=3014904.3014911.

Qiao, F., Yuan, Y., Deng, J., Dai, D., Song, Z., 2016b. Wave-turbulence interaction-induced vertical mixing and its effects in ocean and climate models. Phil. Trans. R. Soc. A 374, 20150201. https://doi.org/10.1098/rsta.2015.0201.

Qiao, F., Wang, G., Khokiattiwong, S., Akhir, M.F., Zhu, W., Xiao, B., 2019. China published ocean forecasting system for the 21st-Century Maritime Silk Road on December 10, 2018. Acta Oceanol. Sin. 38 (1), 1–3. https://doi.org/10.1007/s13131-019-1365-y.

Qiu, W., Ren, F., Wu, L., Chen, L., Ding, C., 2019. Characteristics of tropical cyclone extreme precipitation and its preliminary causes in Southeast China. Meteorog. Atmos. Phys. 131 (3), 613–626. https://doi.org/10.1007/s00703-018-0594-5.

Rajeevan, M., Unnikrishnan, C.K., Bhate, J., Kumar, K.N., Sreekala, P.P., 2012. Northeast monsoon over India: variability and prediction. Meteorol. Appl. 19 (2), 226–236. https://doi.org/10.1002/met.1322.

Rao, R.R., 1986. On the thermal response of the upper eastern Arabian Sea to the summer monsoonal forcing during MONSOON-77. Mausam 37 (7), 77–84.

Rao, D.V.B., 1987. Numerical simulation of tropical-cyclone circulation using Arakawa-Schubert cumulus parameterization. Il Nuovo Cimento C 10 (6), 677–696. https://doi.org/10.1007/BF02507908.

Rao, R.R., Sivakumar, R., 2003. Seasonal variability of sea surface salinity and salt budget of the mixed layer of the North Indian Ocean. J. Geophys Res. Oceans 108 (C1), 3009. https://doi.org/10.1029/2001JC000907.

Sadhuram, Y., Rao, B.P., Rao, D.P., Shastri, P.N.M., Subrahmanyam, M.V., 2004. Seasonal variability of cyclone heat potential in the bay of Bengal. Nat. Hazards 32 (2), 191–209. https://doi.org/10.1023/B:NHAZ.0000031313.43492.a8.

Sadhuram, Y., Murthy, T.R., Somayajulu, Y.K., 2006. Estimation of tropical cyclone heat potential in the bay of Bengal and its role in the genesis and intensification of storms. Indian J. Mar. Sci. 35 (2), 132–138.

Sarma, Y.V.B., Krishna, V.V., Rao, D.P., Sastry, J.S., 1990. Thermohaline circulation and water characteristics around Mauritius group of islands. Indian J. Mar. Sci. 19, 196–200.

Schade, L.R., 2000. Tropical cyclone intensity and sea surface temperature. J. Atmos. Sci. 57 (18), 3122–3130. https://doi.org/10.1175/1520-0469(2000)057%3C3122:TCIASS%3E2.0.CO;2.

Schott, F.A., McCreary Jr., J.P., 2001. The monsoon circulation of the Indian Ocean. Prog. Oceanogr. 51 (1), 1–123. https://doi.org/10.1016/S0079-6611(01)00083-0.

Schott, F.A., Xie, S.P., McCreary Jr., J.P., 2009. Indian Ocean circulation and climate variability. Rev. Geophys. 47 (1), RG1002. https://doi.org/10.1029/2007RG000245.

Sengupta, D., Raj, G.N.B., Shenoi, S.S.C., 2006. Surface freshwater from bay of Bengal runoff and Indonesian throughflow in the tropical Indian Ocean. Geophys. Res. Lett. 33 (22), L22609. https://doi.org/10.1029/2006GL027573.

Sengupta, D., Senan, R., Goswami, B.N., Vialard, J., 2007. Intraseasonal variability of equatorial Indian Ocean zonal currents. J. Clim. 20 (13), 3036–3055. https://doi.org/10.1175/JCLI4166.1.

Sengupta, D., Parampil, S.R., Bhat, G.S., Murty, V.S.N., Babu, V.R., Sudhakar, T., Premkumar, K., Pradhan, Y., 2008. Warm pool thermodynamics from the Arabian Sea monsoon experiment (ARMEX). J. Geophys Res. Oceans 113 (C10), C10008. https://doi.org/10.1029/2007JC004623.

Shee, A., Sil, S., Gangopadhyay, A., Gawarkiewicz, G., Ravichandran, M., 2019. Seasonal evolution of oceanic upper layer processes in the northern Bay of Bengal following a single Argo float. Geophys. Res. Lett. 46 (10), 5369–5377. https://doi.org/10.1029/2019GL082078.

Shenoi, S.S.C., Shankar, D., Shetye, S.R., 2002. Differences in heat budgets of the near-surface Arabian Sea and Bay of Bengal: implications for the summer monsoon. J. Geophys Res. Oceans 107 (C6), 3052. https://doi.org/10.1029/2000JC000679.

Shetye, S.R., Gouveia, A.D., Shankar, D., Shenoi, S.S.C., Vinayachandran, P.N., Sundar, D., Michael, G.S., Nampoothiri, G., 1996. Hydrography and circulation in the western bay of Bengal during the northeast monsoon. J. Geophys Res. Oceans 101 (C6), 14011–14025. https://doi.org/10.1029/95JC03307.

Shu, Q., Qiao, F., Song, Z., Xia, C., Yang, Y., 2011. Improvement of MOM4 by including surface wave-induced vertical mixing. Ocean Model (Oxf) 40 (1), 42–51.

Sprintall, J., Tomczak, M., 1992. Evidence of the barrier layer in the surface layer of the tropics. J. Geophys Res. Oceans 97 (C5), 7305–7316. https://doi.org/10.1029/92JC00407.

Stommel, H.M., 1958. The Gulf Stream: A Physical and Dynamical Description. University of California Press, Berkeley, California.

Subrahmanyam, B., Murty, V.S.N., Sharp, R.J., O'Brien, J.J., 2005. Air-sea coupling during the tropical cyclones in the Indian Ocean: a case study using satellite observations. Pure Appl. Geophys. 162 (8), 1643–1672. https://doi.org/10.1007/s00024-005-2687-6.

Sun, J., Wang, D., Hu, X., Ling, Z., Wang, L., 2019. Ongoing poleward migration of tropical cyclone occurrence over the western North Pacific Ocean. Geophys. Res. Lett. 46 (15), 9110–9117. https://doi.org/10.1029/2019GL084260.

Sun, Y., Perrie, W., Qiao, F., Wang, G., 2020. Intercomparisons of high-resolution global ocean analyses: evaluation of a new synthesis in tropical oceans. J. Geophys Res. Oceans 125 (12). https://doi.org/10.1029/2020JC016118 e2020JC016118.

Thadathil, P., Muraleedharan, P.M., Rao, R.R., Somayajulu, Y.K., Reddy, G.V., Revichandran, C., 2007. Observed seasonal variability of barrier layer in the Bay of Bengal. J. Geophys Res. Oceans 112 (C2), C02009. https://doi.org/10.1029/2006JC003651.

Thadathil, P., Suresh, I., Gautham, S., Kumar, S.P., Lengaigne, M., Rao, R.R., Neetu, S., Hegde, A., 2016. Surface layer temperature inversion in the Bay of Bengal: Main characteristics and related mechanisms. J. Geophys Res. Oceans 121 (8), 5682–5696. https://doi.org/10.1002/2016JC011674.

Thangaprakash, V.P., Girishkumar, M.S., Suprit, K., Kumar, N.S., Chaudhuri, D., Dinesh, K., Kumar, A., Shivaprasad, S., Ravichandran, M., Farrar, J.T., Weller, R.A., 2016. What controls seasonal evolution of sea surface temperature in the bay of Bengal? Mixed layer heat budget analysis using moored buoy observations along 90° E. Oceanogr 29 (2), 202–213.

Usui, N., Ishizaki, S., Fujii, Y., Tsujino, H., Yasuda, T., Kamachi, M., 2006. Meteorological research institute multivariate ocean variational estimation (MOVE) system: some early results. Adv. Space Res. 37 (4), 806–822. https://doi.org/10.1016/j.asr.2005.09.022.

Vinayachandran, P.N., Nanjundiah, R.S., 2009. Indian Ocean Sea surface salinity variations in a coupled model. Clim. Dyn. 33 (2–3), 245–263. https://doi.org/10.1007/s00382-008-0511-6.

Vinayachandran, P.N., Murty, V.S.N., Babu, V.R., 2002. Observations of barrier layer formation in the Bay of Bengal during summer monsoon. J. Geophys Res. Oceans 107 (C12). https://doi.org/10.1029/2001JC000831. SRF-19.

Vinayachandran, P.N., Shankar, D., Vernekar, S., Sandeep, K.K., Amol, P., Neema, C.P., Chatterjee, A., 2013. A summer monsoon pump to keep the Bay of Bengal salty. Geophys. Res. Lett. 40 (9), 1777–1782. https://doi.org/10.1002/grl.50274.

Vincent, E.M., Lengaigne, M., Madec, G., Vialard, J., Samson, G., Jourdain, N.C., Menkès, C.E., Jullien, S., 2012a. Processes setting the characteristics of sea surface cooling induced by tropical cyclones. J. Geophys Res. Oceans 117 (C2), C02020. https://doi.org/10.1029/2011JC007396.

Vincent, E.M., Lengaigne, M., Vialard, J., Madec, G., Jourdain, N.C., Masson, S., 2012b. Assessing the oceanic control on the amplitude of sea surface cooling induced by tropical cyclones. J. Geophys Res. Oceans 117 (C5), C05023. https://doi.org/10.1029/2011JC007705.

Wang, Q., Li, S., Li, R., 2018. Forecasting energy demand in China and India: using single-linear, hybrid-linear, and non-linear time series forecast techniques. Energy 161, 821–831. https://doi.org/10.1016/j.energy.2018.07.168.

Winton, M., 2000. A reformulated three-layer sea ice model. J. Atmos. Ocean. Technol. 17, 525–531.

Wu, L., Rutgersson, A., Sahlée, E., 2015. Upper-ocean mixing due to surface gravity waves. J. Geophys Res. Oceans 120 (12), 8210–8228. https://doi.org/10.1002/2015JC011329.

Wyrtki, K., Bennett, E.B., Rochford, D.J., 1971. Oceanographic Atlas of the International Indian Ocean Expedition. National Science Foundation, Washington, DC.

Xiao, B., Qiao, F., Shu, Q., 2016. The performance of a Z-level ocean model in modeling global tide. Acta Oceanol. Sin. 35 (11), 35–43. https://doi.org/10.1007/s13131-016-0884-z.

Yang, J., Liu, Q., Xie, S.P., Liu, Z., Wu, L., 2007. Impact of the Indian Ocean SST basin mode on the Asian summer monsoon. Geophys. Res. Lett. 34 (2), L02708. https://doi.org/10.1029/2006GL028571.

Zhu, J., Shi, J., Guo, X., Gao, H., Yao, X., 2018. Air-sea heat flux control on the Yellow Sea cold water mass intensity and implications for its prediction. Cont. Shelf Res. 152, 14–26. https://doi.org/10.1016/j.csr.2017.10.006.